

# From pore collapse to crystal growth: ultrafast laser-induced stishovite formation in nanoporous silica

Aram Yedigaryan<sup>1</sup>, Mohamed Yaseen Noor<sup>2</sup>, Elena Kachan<sup>1</sup>, Gabriel Calderon<sup>2</sup>, Jinwoo Hwang<sup>2</sup>, Enam Chowdhury<sup>2</sup>, Jean-Philippe Colombier<sup>1</sup>

<sup>1</sup> *Université Jean Monnet, CNRS, Institut d'Optique Graduate School, Laboratoire Hubert Curien UMR 5516, Saint-Etienne F-42023, France and*

<sup>2</sup> *Department of Materials Science and Engineering, The Ohio State University, 140W 19th Avenue, Columbus, 43210, Ohio, United States*

(Dated: March 19, 2026)

The crystallization of amorphous solids under ultrafast laser irradiation represents a paradigm of non-equilibrium phase transitions, where the interplay between electromagnetic energy localization and atomic-scale dynamics remains largely uncharted. By using a multiscale framework that couples Finite-Difference Time-Domain simulations of nonlinear light propagation with Molecular Dynamics of the atomic response, we demonstrate that field enhancement at nanopore interfaces confines laser energy and drives a rapid collapse of the surrounding matrix. In the silica structure containing a nanopore of 2 nm radius, corresponding to a porosity of approximately 7%, the enhanced local electromagnetic field led to a final equilibrium temperature 16% higher than for the 1-nm pore (1% porosity), and 20% higher than for the homogeneous medium. Particularly, the heterogeneous energy localization in the 2-nm porous system created a preferential nucleation site within the dense glass network and led to the ultrafast formation of stishovite, a high-pressure crystalline phase of SiO<sub>2</sub>, on a sub-nanosecond timescale, significantly faster than in homogeneous silica at the same equilibrium temperature. Such accelerated crystallization enables the phase transition to outpace pressure relaxation, which would otherwise inhibit stishovite formation under identical thermal loading. These predictions align with experimental observations of laser-induced crystallization in confined geometries and establish nanopores as potent catalysts for controlling solid-state transformations via tailored electromagnetic hotspots.

## I. INTRODUCTION

Recreating the extreme conditions of Earth's deep interior in a tabletop experiment is a long-standing challenge in high-pressure physics. Dense silica polymorphs such as stishovite normally form only at pressures of tens of gigapascals and temperatures characteristic of the lower mantle [1–4]. Yet femtosecond lasers can deposit energy so rapidly that comparable thermodynamic states may be reached transiently within a solid. Silica (SiO<sub>2</sub>), the archetypal glass, is uniquely suited to explore this possibility: in its amorphous form it consists of a continuous random network capable of nonlinear absorption, densification, and structural reorganization under ultrafast excitation [5–7]. The central question is therefore not whether extreme states can be reached, but how such fleeting conditions can nucleate and preserve a rare high-pressure crystalline phase before the system relaxes back to disorder.

Femtosecond lasers deposit energy with nanometric confinement and femtosecond precision, driving matter far from equilibrium [8]. In silica, this leads to a rich landscape of responses from smooth refractive-index modification (Type I) to self-organized nanogratings (Type II) and void formation (Type III), with more recent regimes such as Type X and Type C associated with porous and nanocrystalline phases [9–11]. These regimes highlight the extraordinary sensitivity of dielectrics to ultrafast excitation, but they also raise a deeper question: under

what conditions can a transiently heated glass reorganize into a high-pressure crystal?

Although laser-induced crystallization in silica is rare, it has been observed under extreme conditions. Time-resolved X-ray diffraction experiments revealed transient stishovite formation above 18 GPa on nanosecond timescales [12], while molecular dynamics (MD) simulations showed pressure-driven transitions from tetrahedral to octahedral silicon coordination beyond 20 GPa [13]. These results indicate that crystallization is not anomalous, but emerges when local energy density and pressure are sufficiently high. Such conditions are especially relevant in nanoporous systems, where electromagnetic energy can be spatially confined.

Nanoporous structures formed during femtosecond irradiation are now recognized both as a distinct modification pathway and as a source of emergent functionality. Periodic nanopore arrays introduce birefringence and enable photonic applications [10, 14, 15]. Their formation is driven by multiphoton ionization, local field enhancement, and plasma-mediated nanocavitation [16, 17]. Crucially, once created, these pores reshape subsequent light-matter interaction: enhanced local fields and heterogeneous stress relaxation at pore interfaces amplify absorption and can modify crystallization kinetics [18–20]. Whether nanopores merely accompany extreme excitation or actively govern phase selection, however, remains unresolved.

Addressing this question requires a multiscale frame-

work that connects electromagnetic energy localization to atomic-scale structural response. MD provides atomistic insight into nonequilibrium structural evolution [21–27], while the Finite-Difference Time-Domain (FDTD) method captures nonlinear light propagation and field enhancement in complex geometries and interfaces [28–30]. Combined, these approaches enable a unified description of electronic excitation, energy transfer, and lattice reorganization in laser-irradiated dielectrics.

Here, we develop a coupled FDTD-MD framework that self-consistently captures nonlinear light propagation, strong-field photoionization, and energy transfer leading to laser-induced crystallization in nanoporous silica. By explicitly incorporating intensity-dependent bandgap narrowing into the Keldysh photoionization model [31], we demonstrate that electromagnetic confinement at nanopore interfaces generates localized hotspots that drive rapid pore collapse and trigger crystallization into high-pressure stishovite on sub-nanosecond timescales.

This multiscale picture reveals that nanoscale porosity is not a passive byproduct of laser modification but a decisive control parameter in ultrafast phase selection, bridging nonlinear optics, shock physics, and crystallization theory in transparent dielectrics.

## II. MODEL

The major convenient mathematical model widely used in the computational physics community to manage laser-matter interaction at an atomistic scale is the Two-Temperature-Model (TTM) introduced by Anisimov *et al.* [32]. In reality, the theoretical formulation of this model is based on coupling the diffusion equations for electrons and the lattice with the electron-phonon coupling term. Although the TTM takes into account the electronic effects, it is unable to describe thermoelastic stress and lattice density on the atomic level. Therefore, a hybrid model combining these two methods was preferred. Coupling of the atomistic lattice subsystem and the continuum electron subsystem was introduced in many previous works [33–35] and a further modified atomistic-continuum model was described by Ivanov and Zhigilei [36]. The modeling of target response to femtosecond laser irradiation was divided into two parts, the atomistic part which describes the lattice subsystem by MD, and the continuum part which accounts for the processes in the electron subsystem by TTM.

In 2021 a ‘‘Femto3D’’ package was developed [37] based on ‘‘ttm/mod’’ function [38] in Large-scale Atomic/Molecular Massively Parallel Simulator (LAMMPS) [39]. It was designed to model laser ablation in metallic targets and did not take into account nonlinear processes like multiphoton and avalanche ionization in dielectrics and complex geometries. We adapted this package into a more versatile ‘‘Femto3D+’’ package which can be used on metals, semiconductors and dielectrics by including laser source term calculated separately. One

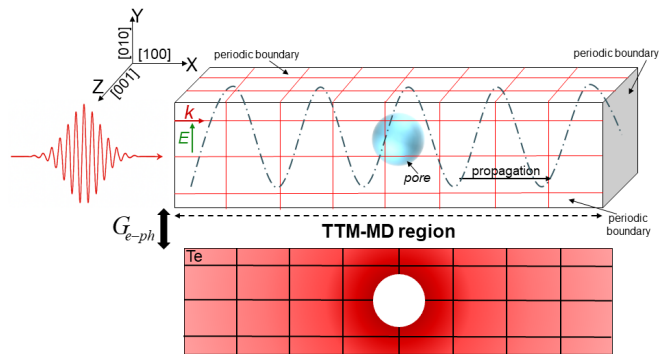


FIG. 1. Schematic representation of the coupled atomistic-continuum framework used in this work. The upper part depicts the lattice (atomic) subsystem, while the lower part represents the electronic subsystem responsible for laser-induced excitation and free-carrier dynamics.

of the approaches is to calculate it via FDTD method, which is the case of our study.

### A. Two-Temperature Model coupled to Molecular Dynamics

The general equations employed for our model are shown as follows:

$$C_e(T_e) \frac{\partial T_e}{\partial t} = \nabla \cdot (K_e(T_e) \nabla T_e) - G_{e-ph}(T_e)(T_e - T_a) + \mathcal{P}(t, \mathbf{r}) \quad (1)$$

$$m_j \frac{d\mathbf{v}_j}{dt} = -\nabla_j U(\mathbf{r}_1, \dots, \mathbf{r}_n) + \mathbf{F}_j^{\text{lang}}(T_e - T_a) \quad (2)$$

In these equations,  $T_e$  and  $T_a$  are the electron and lattice temperatures,  $K_e$  and  $C_e$  are the thermal conductivity and thermal capacity of the electron subsystem,  $G_{e-ph}$  is the electron-phonon coupling factor,  $\mathcal{P}$  is the power density distribution which gives the power loss of the pulse which was absorbed by the medium. For the atom  $j$  in MD,  $m_j$  is the mass of the atom,  $\mathbf{v}_j$  is its velocity, and  $\mathbf{F}_j^{\text{lang}}$  is the Langevin force reflecting the energy transfer from the electronic subsystem. The internal force,  $-\nabla_j U$ , is the force acting on atom  $j$  due to the interatomic potential  $U$ .

Figure 1 shows the scheme of the model. When using fixed periodic boundary conditions, the atoms leaving from one boundary will be reentered into the simulation box from the opposite boundary. In regard of shock wave propagation this will create an effect of shock waves coming from the other similar regions of the medium. This will finally replicate an effect of bulk medium undergone laser irradiation at the peak intensity (we work with a few nm regions). So, fixed periodic boundary condition in all three directions is used for our simulations.

At the atomistic level, the electronic subsystem is treated as a continuous medium that effectively acts as a

thermal reservoir for the atomic system in the MD simulation. Consequently, a canonical ensemble is appropriate for describing the lattice dynamics. Since the electronic temperature evolves at each timestep and the energy exchange between the electronic and lattice subsystems is governed by the coupling factor and their instantaneous temperatures, the Langevin thermostat is a suitable approach for modeling this interaction [37]. The electron-phonon coupling was represented through a stochastic Langevin force, following the formulation introduced by Duffy and Rutherford [40, 41], with the modified expression given as:

$$\mathbf{F}_{\text{lang}} = -\frac{m_i G_{e-ph}(T_e)}{3n_i k_b} \mathbf{v}_T + \sqrt{2k_b T_e \frac{m_i G_{e-ph}(T_e)}{3n_i k_b}} \delta t \boldsymbol{\beta}. \quad (3)$$

Here  $m_i$  is the ionic mass,  $n_i$  is the ionic density of the cell,  $k_b$  is the Boltzmann constant,  $\delta t$  is the timestep used in MD,  $\boldsymbol{\beta}$  is a vector in three dimensions whose components are independent random variables (each with an average 0 and a standard deviation 1), and  $\mathbf{v}_T = \mathbf{v} - \mathbf{v}_c$  with  $\mathbf{v}$  and  $\mathbf{v}_c$  being the velocity of the atom and the center of mass velocity in the corresponding cell, respectively.

In the original model the laser source term used in Eq.(1) (last term of right-hand side) was a temporal-Gaussian distribution with a Beer-Lambert type term to include exponential decay of the intensity in the propagation direction. This behavior, of course, is unsuitable for a transparent dielectric like silica, and a new approach which properly describes the highly nonlinear phenomena like multiphoton and avalanche ionization is used. Thus, we use FDTD simulations to solve nonlinear Maxwell equations and calculate the power loss density in the medium and, finally, include it in Eq.(1).

## B. Finite-Difference Time-Domain

To resolve the spatiotemporal dynamics of laser-matter interaction at the nanometer scale, we employ the FDTD method, which directly integrates Maxwell's equations in space and time [28, 42]. We use the implementation developed in Ref. [43], tailored for nonlinear laser-matter interaction in structured materials.

The Maxwell's curl equations are given as [28]:

$$\begin{aligned} \nabla \times \mathbf{E} &= -\frac{\partial \mathbf{B}}{\partial t}, \\ \nabla \times \mathbf{H} &= \frac{\partial \mathbf{D}}{\partial t}. \end{aligned} \quad (4)$$

where  $\mathbf{E}$  is the electric field,  $\mathbf{H}$  the magnetic field,  $\mathbf{D}$  the electric displacement field,  $\mathbf{B}$  the magnetic induction. The constitutive relations are  $\mathbf{D} = \varepsilon_0 \varepsilon \mathbf{E} + \mathbf{P}$  and  $\mathbf{B} = \mu_0 \mathbf{H}$ , where  $\varepsilon_0$  is the vacuum permittivity,  $\mu_0$  the vacuum permeability, and  $\varepsilon$  the relative permittivity of the medium which represents all the linear nondispersive terms. Relative permeability  $\mu$  is equal to 1 for silica.

Polarization  $\mathbf{P}$  includes all the dispersive terms and nonlinearities relevant at high laser intensities:

$$\begin{aligned} \mathbf{P} &= \mathbf{P}_{disp} + \mathbf{P}_{nl} + \mathbf{P}_p + \mathbf{P}_a, \\ \mathbf{P}_{disp} &= \varepsilon_0 \chi_{disp}^{(1)}(\omega) \mathbf{E}, \\ \mathbf{P}_{nl} &= \varepsilon_0 \chi^{(2)} \mathbf{E}^2 + \varepsilon_0 \chi^{(3)} \mathbf{E}^3, \end{aligned} \quad (5)$$

where  $\mathbf{P}_{disp}$  is a dispersive polarization from dispersive materials such as Lorentz media [28],  $\mathbf{P}_{nl}$  is the nonlinear term, and  $\mathbf{P}_p$  and  $\mathbf{P}_a$  are auxiliary polarizations defining the Drude plasma and the multiphoton absorption, respectively.

The plasma current density  $\mathbf{J}_p$  follows directly from the time derivative of the plasma polarization  $\mathbf{P}_p$ :  $\mathbf{J}_p = \frac{\partial \mathbf{P}_p}{\partial t}$ . It is the continuous-time Drude current driven by the field in a collisional electron gas, and can thus be given as:

$$\frac{\partial^2 \mathbf{P}_p}{\partial t^2} + \nu_c \frac{\partial \mathbf{P}_p}{\partial t} = \frac{e^2}{m_e} n_e \mathbf{E}, \quad (6)$$

where  $e$  is the electron charge,  $m_e$  the electron mass,  $\nu_c$  the electron collision frequency, and  $n_e$  the free-electron density.

The multiphoton ionization current can be given via  $\mathbf{P}_a$  as:

$$\frac{\partial \mathbf{P}_a}{\partial t} = K \hbar \omega_0 \frac{\partial n_e}{\partial t} \frac{\mathbf{E}}{|\mathbf{E}|^2} \quad (7)$$

where  $K$  is the number of photons absorbed, and  $\omega_0$  is the photon central angular frequency.

The carrier density obeys a nonlinear rate equation including Keldysh photoionization and field-driven impact ionization, enabling feedback between local field enhancement and plasma generation:

$$\frac{\partial n_e}{\partial t} = W_{pi}(I) (n_0 - n_e) + R_{ai} |\mathbf{E}|^2 n_e, \quad (8)$$

where  $n_0$  is the initial number of valence electrons, and  $R_{ai}$  is written in terms of a collisional absorption cross-section and the bandgap  $U_i$ ,

$$R_{ai} = \frac{\sigma_B}{U_i}, \quad \sigma_B = \frac{q_e^2}{m_e} \frac{\nu_c}{\nu_c^2 + \omega_0^2}, \quad (9)$$

with  $\sigma_B$  being the inverse Bremsstrahlung absorption cross-section.

Figure 2 shows the photoionization rate  $W_{pi}$  (bottom panel) obtained by the Keldysh formalism, where we included the dynamic evolution of bandgap with laser intensity. At first, we calculate the free electron density with Keldysh theory for a constant gap for a big intensity range. Then we use the DFT-derived data of free electron density versus bandgap from Ref. [44] to obtain the bandgap evolution over the intensity. Finally, we use this intensity-dependent bandgap evolution to calculate the photoionization rate. Incorporating the bandgap

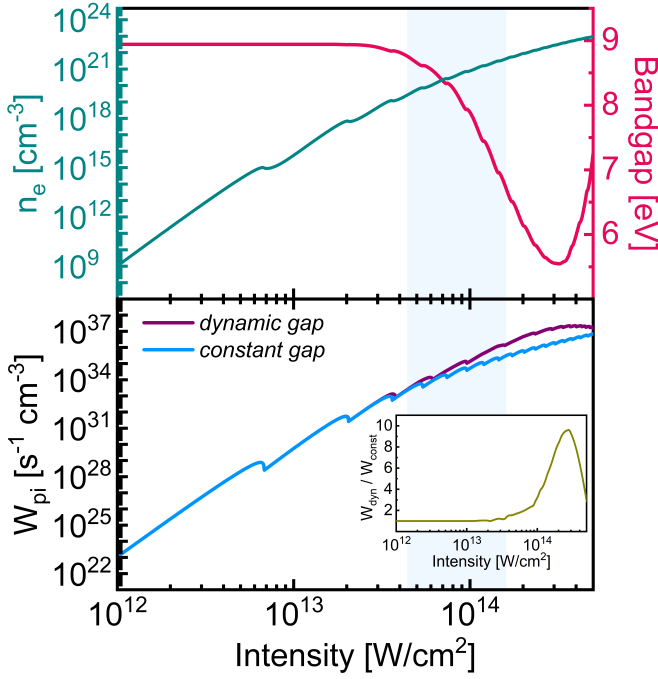


FIG. 2. Photoionization rate (bottom panel) calculated with Keldysh formalism with dynamic and constant bandgap. The inset in bottom panel shows the smoothed ratio  $W_{dyn}/W_{const}$  between ionization rates for dynamic and constant bandgap (8.9 eV), respectively. The top panel shows the free electron density calculated with Keldysh theory for  $\lambda = 1030$  nm and  $\tau = 25$  fs for the same intensity range, and this density-corresponding bandgap evolution taken from Ref. [44] to derive the intensity-bandgap relation used in ionization rate calculation in bottom panel. The light gray area indicates the intensity range used in FDTD simulations.

change, which accounts for ultrafast charge redistribution and electron-electron screening, into the Keldysh kernel, reflects the physical reality that under femtosecond excitation, the conduction-band population transiently modifies the electronic potential, leading to a reversible narrowing of the bandgap down to about 5.5 eV.

The inset in bottom panel shows the smoothed ratio  $W_{dyn}/W_{const}$  between ionization rates for dynamic and constant bandgaps (8.9 eV), respectively. The top panel shows the free electron density and bandgap evolution [44] for the same intensity range. The results reveal that the ratio between ionization rates begins to rise at intensities above  $2 \times 10^{13}$  W/cm<sup>2</sup>, when the bandgap starts to shrink, peaks around  $3 \times 10^{14}$  W/cm<sup>2</sup> with a maximum value of approximately 10, and then gradually decreases to  $\sim 3$ .

By denoting  $\tilde{\mathbf{D}} = \mathbf{D} - \mathbf{P}_{disp} - \mathbf{P}_p - \mathbf{P}_a$ , we can give the instantaneous isotropic or diagonal anisotropic nonlinear effects of the form:

$$\tilde{D}_i = \varepsilon_0 \varepsilon E_i + \varepsilon_0 \chi_i^{(2)} E_i^2 + \varepsilon_0 \chi_i^{(3)} |\mathbf{E}|^2 E_i, \quad (10)$$

Instead of implementing this equation directly, which would require to solve a cubic equation at each time step,

the code uses the following Padé approximation which matches the cubic solution to high-order accuracy [29]:

$$E_i = \left[ \frac{1 + \frac{\varepsilon_0 \chi^{(2)}}{[\varepsilon_0 \varepsilon]^2} \tilde{D}_i + 2 \frac{\varepsilon_0 \chi^{(3)}}{[\varepsilon_0 \varepsilon]^3} \|\tilde{\mathbf{D}}\|^2}{1 + 2 \frac{\varepsilon_0 \chi^{(2)}}{[\varepsilon_0 \varepsilon]^2} \tilde{D}_i + 3 \frac{\varepsilon_0 \chi^{(3)}}{[\varepsilon_0 \varepsilon]^3} \|\tilde{\mathbf{D}}\|^2} \right] [\varepsilon_0 \varepsilon]^{-1} \tilde{D}_i. \quad (11)$$

In Maxwell's equations, the power density  $\mathcal{P}$  drawn from the field to the medium can be given through the plasma current by  $\mathcal{P} = \mathbf{J}_p \cdot \mathbf{E}$ . This power density  $\mathcal{P}$  is what we finally insert as the source term in Eq.(1).

### C. Setup

To model the post-compression state of silica following laser-induced shock wave propagation, we initialized our amorphous system at a density of  $\sim 4.3$  g/cm<sup>3</sup>, corresponding to stishovite density at elevated pressure. This state represents shock-compressed amorphous silica immediately prior to crystallization, bypassing the initial compression phase which occurs on timescales and length scales beyond current MD capabilities. Starting from a stishovite unit cell ( $a = 4.17$  Å,  $c = 2.66$  Å), we created a small supercell of 1350 atoms and amorphized it by heat-anneal-quench-relax protocol, which yields a structurally amorphous but dense silica, analogous to the material state observed in laser-compressed regions prior to crystallization [12, 45, 46]. It was heated to 8000 K to ensure complete amorphization while maintaining high density, annealed for 0.5 ns, then quenched back to 300 K, followed by a final relaxation phase for another 0.5 ns. The resulting structure was then replicated again and relaxed to obtain a supercell of a few hundred cubic nanometer volume. A nanopore with a radius of 2 nm was finally created in the center. This final state, which is a dense amorphous nanocuboid with a nanopore in the center, is our main TTM-MD system undergone laser irradiation. Another similar supercell with a pore with a twice smaller radius (1 nm) was created as well for comparison with the original system.

The resolution used for FDTD simulations was 0.125 nm. After the distributions were obtained, they were interpolated to the MD resolution, which in our simulations was 0.95 nm. This is considered a minimum resolution for TTM-MD simulations because smaller cell size could lead to incorrect energy gradients, over/under-heated cells, wrong dynamics and simulation crash. The refractive index used was 1.45. The neutral electron density was  $3.5 \times 10^{23}$  cm<sup>-3</sup>, and the collision frequency was  $4.29 \times 10^{13}$  s<sup>-1</sup> [47]. The reduced effective mass used for Keldysh theory was  $0.64m_e$  [48]. Since the structure length is very small compared to wavelength, the dispersion is negligible ( $\chi_{disp}^{(1)}(\omega) = 0$ ).  $\chi^{(2)} = 0$  due to centrosymmetry in silica, and for the third-order susceptibility we took  $\chi^{(3)} = 2.5 \times 10^{-22}$  m<sup>2</sup>/V<sup>2</sup> [49]. The intensity of the Gaussian pulse used was  $I = 10^{14}$  W/cm<sup>2</sup>,

the wavelength was  $\lambda = 1030$  nm, and the pulse duration was  $\tau = 25$  fs at full-width half-maximum (FWHM).

The electronic specific heat  $C_e(T_e)$  and electron-phonon coupling factor  $G_{e-ph}(T_e)$ , used in Eq.(1), were taken from a recent study by Tsaturyan *et al.* which investigates ultrafast laser excitation of  $\alpha$ -quartz by applying high electron temperature according to Fermi-Dirac distribution of electrons using density functional theory (DFT), GW approximation, and density functional perturbation theory (DFPT) to extract a full set of electronic properties under excitation [44]. The bandgap, which was shown to shrink at high intensities from the initial  $\sim 8.9$  eV down to  $\sim 5.5$  eV, followed by a rise at very high temperatures due to competing Hartree and exchange-correlation effects, was used to calculate the ionization rate depending on the dynamic bandgap via Keldysh theory, as shown in Fig. 2, with the latest feeding Eq.(8). The electronic thermal conductivity  $K_e(T_e)$  was calculated as in Ref. [50].

As an interatomic potential in MD the modified BKS (Beest-Kramer-Santen) potential was used [51]. All MD simulations are carried out by LAMMPS [39]. Visualization is performed by OVITO [52].

### III. RESULTS

We now demonstrate how nanoscale porosity governs laser energy localization, pore collapse, and ultimately rare-phase crystallization in silica through coupled FDTD-TTM-MD simulations.

Figure 3(a) shows the amorphous nanocuboid obtained in MD after replication and thermalization of the smaller amorphous supercell. Fig. 3(b) shows a 1-nm-thick central slice after the creation of the nanopore. The same procedure was later used to obtain a similar structure but with a nanopore of twice smaller radius (1-nm).

Figure 3(c) shows the energy density distribution obtained from the FDTD simulation for a structural geometry as in Fig. 3(b). Similar FDTD simulation at the same intensity and laser parameters was repeated for the 1-nm pore system (Fig. 3(d)) and for a homogeneous (no pore) system. The spatial energy distributions reflect the propagation of the incident pulse along the X-direction and its linear polarization along Y, leading to a strongly anisotropic absorption pattern. Because the electric field oscillates along Y, the dielectric discontinuity at the silica-pore interface induces polarization charges whose magnitude depends on the local surface curvature and field orientation. As a result, the tangential field components remain continuous across the interface, while the normal component of the displacement field must satisfy boundary conditions that enhance the electric field inside the high-index region near the pore boundary. This mismatch in permittivity produces localized field amplification, particularly at the equatorial regions of the pore aligned with the polarization axis. The amplified near-fields increase the local intensity and,

through the nonlinear photoionization response, generate highly concentrated free-electron densities and absorption hotspots. These electromagnetic hotspots are absent in the homogeneous system and constitute the primary source of spatially localized energy deposition that seeds subsequent thermomechanical evolution. The spatial distributions of free-electron density, laser intensity, and dynamic bandgap are provided in the Supplementary Material.

Figure 3(e) presents the temporal evolution of the 2-nm pore system average electronic temperature  $T_e$  and atomic (lattice) temperature  $T_a$  within the TTM-MD simulation domain during the first few picoseconds following femtosecond laser irradiation. The data clearly demonstrates the characteristic nonequilibrium thermal dynamics described by TTM. At around 75 fs, coinciding with the peak of the incident laser Gaussian electric field envelope, the electrons absorb a large amount of energy, causing a sharp and rapid rise in  $T_e$  to nearly 20000 K. This is followed by a steep decay in  $T_e$  over the next couple of picoseconds, driven by electron-phonon coupling, through which the excited electrons transfer their energy to the lattice.

The temperature evolution also explains the dynamics of the pore collapse observed in the snapshots in Fig. 3(f). The snapshots show the dynamics of the pore of a 1-nm thick central slice during the first picosecond following the ultrafast energy deposition. With peak energy density concentrated near the pore walls due to local field enhancement, the surrounding silica matrix experiences a rapid and intense increase in temperature and pressure. This creates a steep pressure gradient between the heated shell around the pore and the pore interior. As a result, atoms from the high-pressure shell begin to move inward, initiating the collapse of the pore. During the first 0.1 ps, limited electron-phonon coupling prevents significant lattice heating, and the pore remains largely unchanged. However, the electron-phonon coupling gets strong after 0.1 ps and the pore starts to shrink gradually, with the pore volume decreasing significantly by 0.3 ps. By 0.9 ps, the pore has nearly vanished, creating an inhomogeneous structure in terms of temperature, pressure and atomic density in the simulation box and the equilibrium between electronic and atomic system still goes on. This behavior is characteristic of thermomechanical response under extreme non-equilibrium conditions, where the rapid conversion of absorbed optical energy into kinetic motion drives material rapid flow into the pore. The presence of strong heterogeneous temperature and pressure near the pore surface may further accelerate collapse via localized momentum transfer. The simulation thus captures the early-stage pore collapse dynamics that arise from energy focusing effects typical in nanoporous media under ultrafast laser excitation.

Simultaneously,  $T_a$  rises gradually as the phonon system absorbs the transferred energy. By approximately 2-2.5 ps, the two subsystems reach thermal equilibrium at a common temperature, indicating the end of the nonequi-

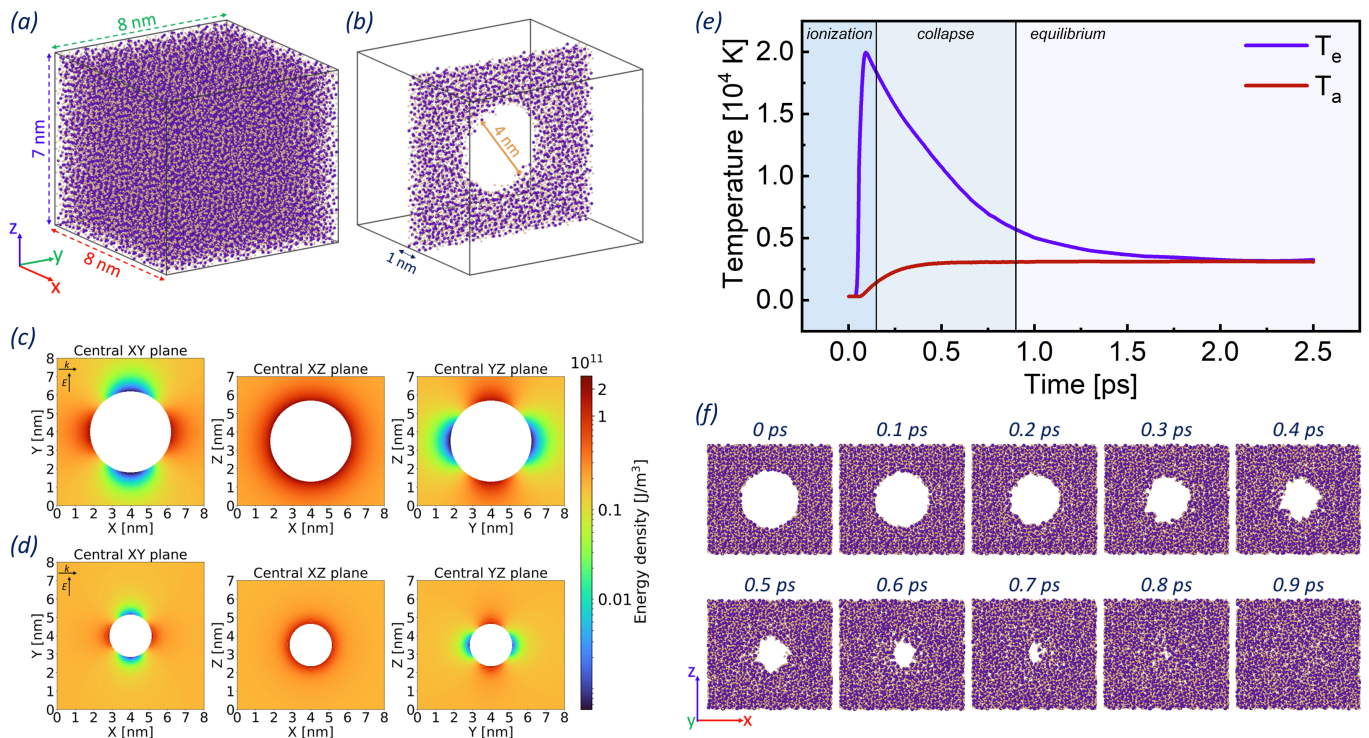


FIG. 3. (a) Amorphous silica nanocuboid obtained after replication and prior to nanopore creation. (b) Central 1-nm-thick slice along the  $x$  direction after introducing a nanopore with radius 2 nm. The simulation cell has a volume of  $\sim 450$  nm<sup>3</sup>, corresponding to a porosity of about 7%. (c,d) Central slices of the absorbed energy density distribution obtained from FDTD simulations for nanopores with radii of (c) 2 nm and (d) 1 nm, showing strong energy localization near the pore boundary. The laser wavelength, pulse duration, and peak intensity are 1030 nm, 25 fs, and  $10^{14}$  W/cm<sup>2</sup>, respectively. (e) Temporal evolution of the average electronic and atomic temperatures during the first few picoseconds following laser excitation. (f) Snapshots of a central 1-nm-thick slice of the simulation box during the first picosecond, showing the onset of laser-driven nanopore collapse.

librium regime. After this point, both  $T_e$  and  $T_a$  remain nearly constant, at an equilibrated temperature of around 3100 K, confirming that no further external energy input is present and that internal thermal exchange has completed. In case of the structure with a 1-nm pore (Fig. 3(d)) the system equilibrated at a final temperature of 2670 K, which is approximately 14% less than in case of 2-nm system. The final equilibrium temperature for the homogeneous system (no pore) was 2580 K, 17% less than the 2-nm system and only 3% less than the 1-nm system.

The difference in the final equilibrium temperatures among the three systems arises from the varying degree of local field enhancement caused by the pore size. In the structure with a 2-nm pore, the curvature and dielectric contrast around the pore strongly amplify the local electric field during laser irradiation. This leads to higher energy absorption and, consequently, a higher post-irradiation temperature of about 3100 K. In the case of the 1-nm pore, it is smaller and supports less efficient confinement of the electromagnetic field. As a result, the absorbed energy and the final temperature of 2670 K are both lower, approaching that of the homogeneous structure (2580 K). The small temperature difference between the 1-nm and homogeneous systems indicates that

sub-nanometer porosity contributes only marginally to energy localization under these irradiation conditions. Since the equilibrium temperatures of the 1-nm and homogeneous systems remain well below the threshold required for a phase transition at the given ionic density, no structural transformation was observed even after several nanoseconds. Therefore, from now on, only the 2-nm pore system, where the transition occurred, is discussed in detail.

Figure 4 presents snapshots of the atomic configuration during the crystallization stage. The first row shows the full simulation box, the second row a central subregion of approximately 3 nm, and the third row an even smaller region extracted from this central volume to highlight the emerging crystalline order. At 0.7 ns, only faint traces of crystalline ordering are visible in the full simulation box, becoming more pronounced by 0.8 ns. In contrast, the cut regions reveal the onset of crystallinity earlier, around 0.6 ns, as expected given that nucleation occurs stochastically at localized sites rather than simultaneously throughout the system. Within  $\sim 0.5$  ns, the crystalline front propagates through most of the simulation cell. By 1.1 ns the system has largely transformed into the crystalline stishovite phase, although structural relaxation continues for several tens of nanoseconds as

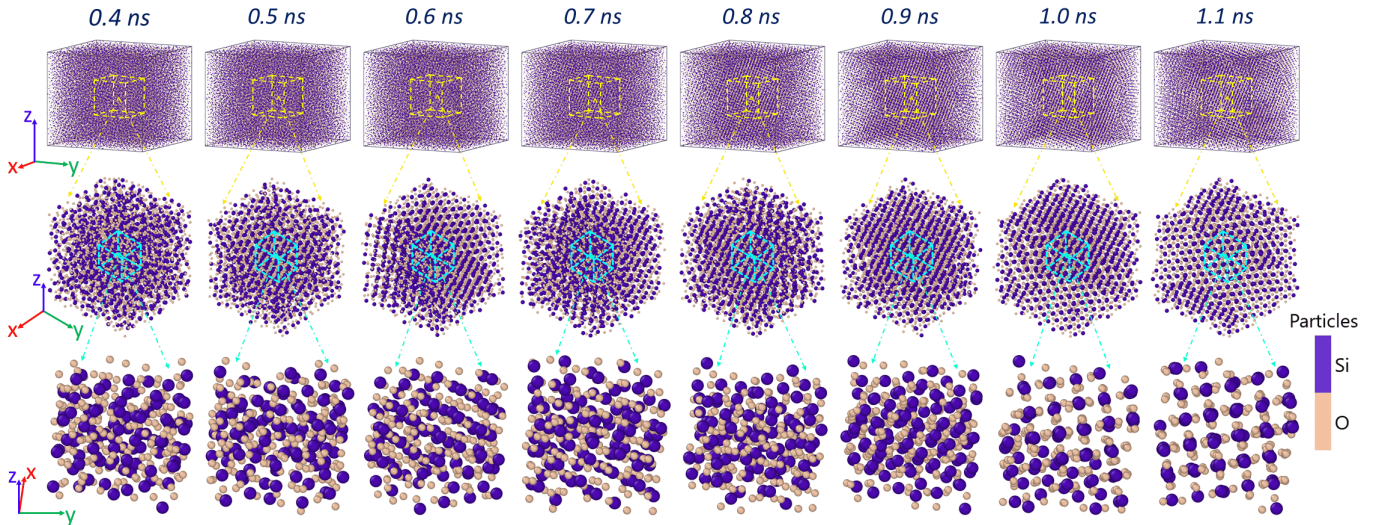


FIG. 4. Snapshots of the simulation cell at successive times during crystallization. The first row shows the full simulation box, the second row a central cuboid region of approximately 3 nm per side, and the third row a smaller subsection extracted from this region to highlight the emerging crystalline order. Minor differences between adjacent snapshots may arise from atomic motion across periodic boundaries, which can slightly shift the apparent lattice alignment between frames.

the lattice progressively minimizes its energy. Residual thermal fluctuations remain visible in the final snapshot of the third row in Fig. 4. Minor differences between neighboring snapshots can also arise from atomic motion across periodic boundaries, which may slightly shift the apparent lattice features between frames.

The nucleation and crystallization process is further elucidated by examining the system potential energy and pressure evolution. Fig. 5 presents the time-dependent behavior of both quantities after the thermal equilibration. As shown in the figure, a slow decrease in both potential energy and pressure begins at around 0.35 ns, marking the onset of critical nucleus formation which leads to crystallization. Around 0.5 ns the decrease in both quantities becomes abrupt, a characteristic signature of a first-order phase transition. This indicates that the system has crossed the nucleation threshold and entered a rapid transformation toward the crystalline stishovite phase. The sharp drop in potential energy by  $\sim 0.27$  eV/atom is accompanied by a pressure drop of  $\sim 14$  GPa, consistent with the collapse of the disordered structure into an energetically more favorable configuration. This transition occurs within a narrow time window of around 0.5 ns, signifying that crystallization proceeds instantaneously once a critical nucleus forms. After around 1.1 ns the drop in potential energy and pressure slows down, indicating that the phase transition has finished, which closely match the timeframes of the crystallization snapshots seen in Fig. 4. However the decrease in potential energy and pressure still continues to up to tens of nanoseconds until the system finds the minimum, energetically most favorable state.

To assess the structural similarity between the crystallized system and the pure stishovite crystal, we computed partial radial distribution functions (PRDFs) for Si-Si,

Si-O, and O-O atomic pairs (Fig. 6). The pure stishovite crystal was replicated and heated to the equilibration temperature of laser irradiated structure to get rid of the thermal noise effects when comparing the PRDFs. The PRDF of amorphous silica at the stishovite density and at the same temperature is shown as well for comparison between the crystalline and disordered phases. As shown in Fig. 6, the peak positions for all three pairs match almost perfectly between the crystallized system and pure stishovite. This close agreement provides strong evidence that the crystallized system has indeed adopted the stishovite phase. In contrast to the crystalline phase, the PRDFs of the amorphous structure exhibit significantly broader and less pronounced peaks. This reflects the lack of long-range periodicity and the presence of local structural disorder. While the first-neighbor peak is typically still visible, indicating short-range order, the higher-order coordination shells are smeared out or entirely absent, consistent with the random network topology of amorphous silica.

However, even though the PRDFs of the crystallized and pure stishovite systems overlay each other perfectly for Si-O and O-O pairs, the peaks' amplitudes are slightly different for the Si-Si pair. For numerical comparison the root mean square deviation (RMSD) between the PRDFs were calculated for all three pairs. The RMSD values of 8% for Si-O and 5% for O-O pairs indicate a strong preservation of the local bonding environment. The first-neighbor peaks in all RDFs are in excellent agreement, suggesting minimal disruption of short-range order. In contrast, the Si-Si partial RDF exhibits a notably higher RMSD of 23%. While the first two Si-Si peaks, representing the immediate and second silicon neighbors, align well in both position and intensity, discrepancies emerge in the subsequent coordination shells. These deviations

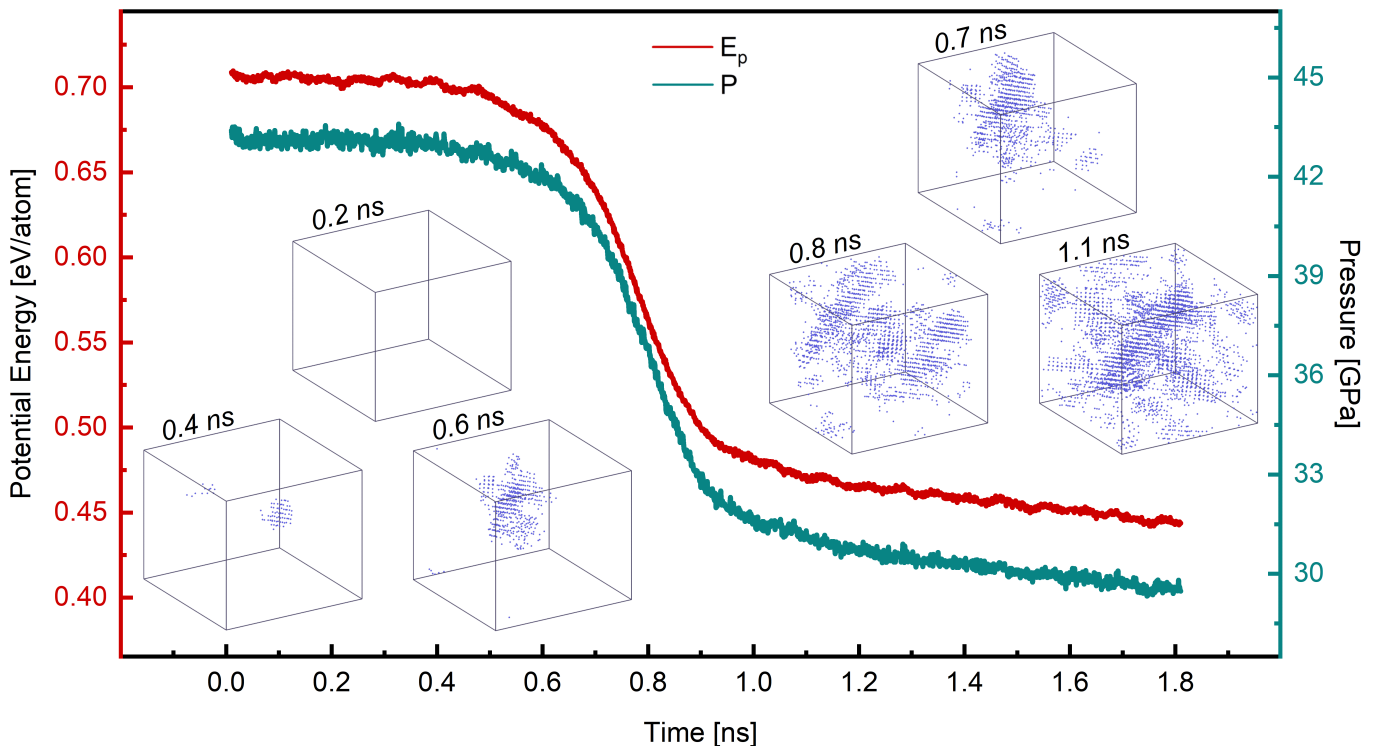


FIG. 5. Temporal evolution of the potential energy per atom and pressure after thermal equilibration. The decrease of both quantities signals the onset of the phase transition. Insets show atomic snapshots illustrating the nucleation and growth of stishovite-like clusters (Si atoms only).

are not due to changes in bond distances alone but are instead attributed to distortions in medium- and long-range order, discussed in detail in the following section.

#### IV. DISCUSSION

The thorough investigation of the obtained configurations revealed three main reasons for the distortions in Si-Si pair PRDF. The first reason is that the distorted structure maintains the stishovite topology but has undergone a reorientation of its crystallographic axes. Specifically, the *c*-axis of the distorted structure no longer aligns with the original [001] direction of the simulation box but is instead oriented along a nontrivial direction, forming oblique angles with the simulation cell axes. This crystallographic misalignment, which is assumed to arise from the random nucleation events, alters the spatial distribution of Si-Si distances beyond the first coordination shell, leading to broadened or asymmetric RDF peaks, despite their positions remaining equal to those of the reference.

The second reason is that a precise comparison of PRDFs requires identical number of atoms in the two structures. However, the reference stishovite was created by replicating a small, thermally equilibrated crystalline unit to ensure periodicity, which limits the number of atoms to integer multiples of that unit. In contrast, the

crystallized structure originates from a nanoporous system, where atoms were removed in a spherical volume, resulting in this structure not being a multiple of a smaller crystalline unit. In our comparison the total atom count for the crystallized system was approximately 6% lower than the reference. This difference affects the normalization of the RDF and introduces amplitude discrepancies, especially in Si-Si pairs that are more sensitive to system size and connectivity.

And last, the removal of atoms to create a nanopore inevitably perturbs the local stoichiometry. This imbalance, combined with independent nucleation effects, can lead to the formation of structural defects such as interstitials, Frenkel pairs, stacking faults, grain boundaries, etc. These imperfections are particularly disruptive to the long-range order probed by the Si-Si PRDF, where coordination shells depend on precise lattice periodicity. Even in perfectly stoichiometric systems, defects may still arise from the convergence of multiple growing crystallites, whose random orientations and mismatch at interfaces produce disorder beyond the first few atomic shells.

Finally, to explore the effect of structural inhomogeneity on the post-laser dynamics and crystallization behavior, another additional set of simulations was performed. The aim was to systematically compare configurations containing a nanopore of varying size with a homogeneous system. The methodology followed the same procedure as before: for each configuration correspond-

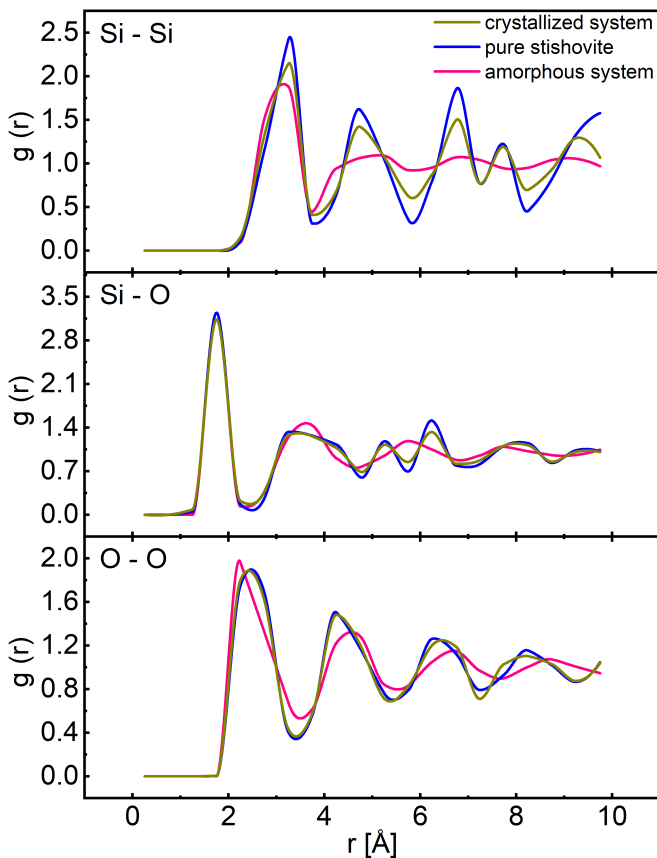


FIG. 6. Partial radial distribution functions for Si-Si, Si-O, and O-O atomic pairs in the crystallized system, compared with those of pure stishovite and amorphous silica under identical thermodynamic conditions, confirming the structural signature of the stishovite phase.

ing FDTD simulations were conducted under identical laser conditions, but the laser intensity was adjusted in each case to achieve comparable energy deposition profiles that would bring the systems to the same thermal (3100 K) and average density ( $4.35 \text{ g/cm}^3$ ) conditions after equilibrium. This allowed us to directly compare the dynamics of crystallization across all three geometries under equivalent thermal loading. In case of 1-nm-pore system the behavior was similar: the pressure initially rose due to rapid energy absorption and thermal expansion, followed by a gradual drop beginning at approximately 0.4 ns. Around 0.5 ns, the pressure drop accelerated sharply, signifying a rapid phase transformation into a crystalline structure which completed around 1.1 ns, as also confirmed through direct visualization of atomic configurations just like before. Interestingly, the similarity in the temporal evolution between the 1-nm and 2-nm pore cases suggests that within this size range, the specific radius of the nanopore does not significantly affect the crystallization kinetics. This implies that even small inhomogeneities are sufficient to seed local fluctuations that can facilitate early nucleation.

In contrast, the homogeneous structure shows notice-

ably different behavior. Here, the drop in pressure and potential energy, signifying critical nucleus formation, only began around 0.85–0.9 ns, more than twice as late as in the porous cases. This delay can be attributed to the absence of pre-existing inhomogeneities, which otherwise act as natural sites for energy localization and nucleation. In a structurally uniform medium, the system must rely on spontaneous thermal fluctuations to initiate crystallization. This process is statistically less probable and slower, resulting in a delayed onset of phase transformation. These findings support the broader view that localized structural or compositional inhomogeneities, such as pores, density fluctuations, or bond distortions, can significantly reduce the energy barrier for nucleation, thereby accelerating the overall crystallization process. These results establish that nanoscale porosity serves as a heterogeneous nucleation seed, dramatically reducing the incubation time for crystallization. The acceleration of nucleation appears largely insensitive to pore size within the 1–2 nm range investigated, suggesting that even minimal nanoscale inhomogeneities are sufficient to trigger this effect. Whether this behavior extends to pores with radii significantly larger than those considered here, where altered field enhancement, pressure confinement, or thermal diffusion may modify nucleation kinetics, remains unexplored.

In classical nucleation theory [53], the nucleation rate depends exponentially on the free-energy barrier for forming a critical nucleus, which reflects the competition between interfacial energy and the thermodynamic driving force. Temperature affects the rate through thermal activation and its influence on both the driving force and kinetic factors. The presence of inhomogeneities, such as pores, interfaces, or compositional gradients, can significantly reduce the nucleation barrier accelerating the process. Nanopores introduce localized regions of high pressure and temperature gradients, due to the laser energy focusing around the pore and its subsequent rapid collapse. These gradients create favorable conditions for atomic rearrangements and may locally alter the chemical potential, driving the system out of equilibrium and promoting faster formation of critical nuclei.

Moreover, the collapse of the pore itself is a strongly nonequilibrium process that leads to a localized spike in pressure and temperature. Such localized transients may induce a heterogeneous nucleation site, facilitating rapid crystalline phase formation. The results are reminiscent of the findings by Poumellec et al., who demonstrated that electric fields induced by laser pulses could locally modulate the chemical potential and favor glass-to-crystal transitions in silica [54]. These phenomena, enhanced by the spatial inhomogeneities, indicate that localized structural fluctuations, like coordination number distributions, broken rings or trapped molecular species, could substantially modify the thermodynamic and kinetic landscape of crystallization.

Additionally, pressure and potential energy are well-known indicators of phase transition dynamics in MD

simulations. The observed two-stage behavior, i.e., a gradual initial drop followed by a sharp drop, aligns with the theoretical picture where the initial slow phase corresponds to the formation and stabilization of critical nuclei, and the subsequent rapid drop indicates a collective phase transformation. The delay observed in the homogeneous case further reinforces the notion that the pore serves as a structural seed or perturbation that drives the system toward crystallization at an accelerated rate. These observations not only validate the physical relevance of our model system but also offer insights into tailoring crystallization kinetics through nanostructuring in experimental settings.

This behavior can be rationalized in light of our experimental observations presented in Sec. V, which reveal that most crystallized regions in laser-irradiated silica glass are localized near interfaces rather than in the bulk. These interfacial zones exhibit enhanced thermal and pressure gradients, localized density fluctuations, and geometric complexity. Such features can locally reduce the nucleation energy barrier by altering the free energy landscape, thereby facilitating the crystallization process.

In addition to spatial inhomogeneities, the dynamics of cooling plays a crucial role. In laser-irradiated systems, the heating phase is extremely rapid, driven by femtosecond to picosecond energy deposition, while the subsequent cooling is significantly slower. In MD simulations, it is computationally infeasible to model realistic cooling rates, which would occur over nanoseconds to microseconds in experiments. In our model, the simulation box is small and positioned at the center of the laser pulse, where the intensity is assumed to be maximal. Consequently, the rate of energy loss is minimized, and we simulate a quasi-isolated system in which most absorbed energy remains within the material. This setup allows us to observe crystallization under idealized, high-energy retention conditions, even though such behavior is more difficult to realize experimentally in homogeneous media.

These considerations help to explain why homogeneous silica is experimentally harder to crystallize compared to inhomogeneous structures. While each polymorph has a specific combination of temperature, pressure and density at which nucleation is thermodynamically favorable, the transition still requires overcoming an activation barrier. After laser excitation, the material transitions into a high-temperature, high-pressure melt that begins to cool gradually. At some point during this cooling, local conditions pass through the thermodynamic window optimal for nucleation. However, this window is temporally narrow. In homogeneous regions, where the nucleation barrier remains relatively high, the system often fails to form a critical nucleus within this time window and continues cooling into a non-crystalline glassy state. In contrast, interfacial or porous regions, due to their lower effective nucleation barriers, are more likely to initiate crystallization during this brief favorable interval.

This framework aligns with our simulation results,

where crystallization in homogeneous silica started more than twice as late as in porous systems, despite identical thermodynamic endpoints. It also explains our experimental finding that crystals preferentially emerge near interfaces, where local inhomogeneities enhance both energy localization and nucleation probability.

In conclusion, this comparative study strongly supports the notion that initial structural inhomogeneities, particularly nanopores, play a crucial role in accelerating crystallization dynamics in laser-irradiated amorphous silica. They not only provide energetically favorable sites for nucleation but also facilitate local stress redistribution and energy dissipation that improve the thermodynamic pathway toward crystallization. These results highlight the importance of considering sub-nanometer scale features when modeling ultrafast phase transformations in disordered materials.

## V. EXPERIMENTS

Amorphous  $\text{SiO}_2/\text{HfO}_2$  multilayer dielectric mirror (MLD) samples were irradiated using femtosecond laser pulses at 1030 nm, with pulse duration of 70 fs. All measurements discussed here correspond to single-pulse laser-matter interactions, enabling direct isolation of ultrafast damage-initiation and phase-transformation mechanisms without cumulative or incubation effects. The complete laser system, irradiation geometry, damage protocol, surface-morphology characterization, and sample preparation procedures for transmission electron microscopy (TEM) are described in detail in our prior works [45, 55]. Site-specific cross-sectional lamellae from laser-modified (blistered) regions were prepared by focused ion beam milling with protective Pt capping and thinned to  $\sim 100$  nm for TEM analysis. Structural characterization was performed using bright-field and high-resolution TEM imaging, selected-area electron diffraction (SAED), and four-dimensional scanning transmission electron microscopy (4D-STEM). SAED patterns acquired from sub-micrometer regions were indexed by comparing measured  $d$ -spacings with simulated diffraction patterns, while 4D-STEM nano-diffraction datasets were obtained by raster-scanning a focused probe and recording a full diffraction pattern at each position, enabling spatially resolved phase identification within the laser-modified volume.

Figure 7 illustrates the nanoscale structural evolution induced at the  $\text{SiO}_2/\text{HfO}_2$  interface of the MLD mirror following femtosecond laser irradiation. Fig. 7(a) is the cross-sectional TEM image of the laser-modified multilayer stack showing pronounced interfacial damage morphology. In addition to layer distortion and blister formation as reported in Ref. [55], a nanoporous region is observed in the  $\text{SiO}_2$  and  $\text{HfO}_2$  layers, as highlighted in the inset in Fig. 7(a). This region consists of nanoscale voids and density fluctuations extending laterally along the interface, indicative of rapid volumetric expansion and material rarefaction following ultrafast energy deposition.

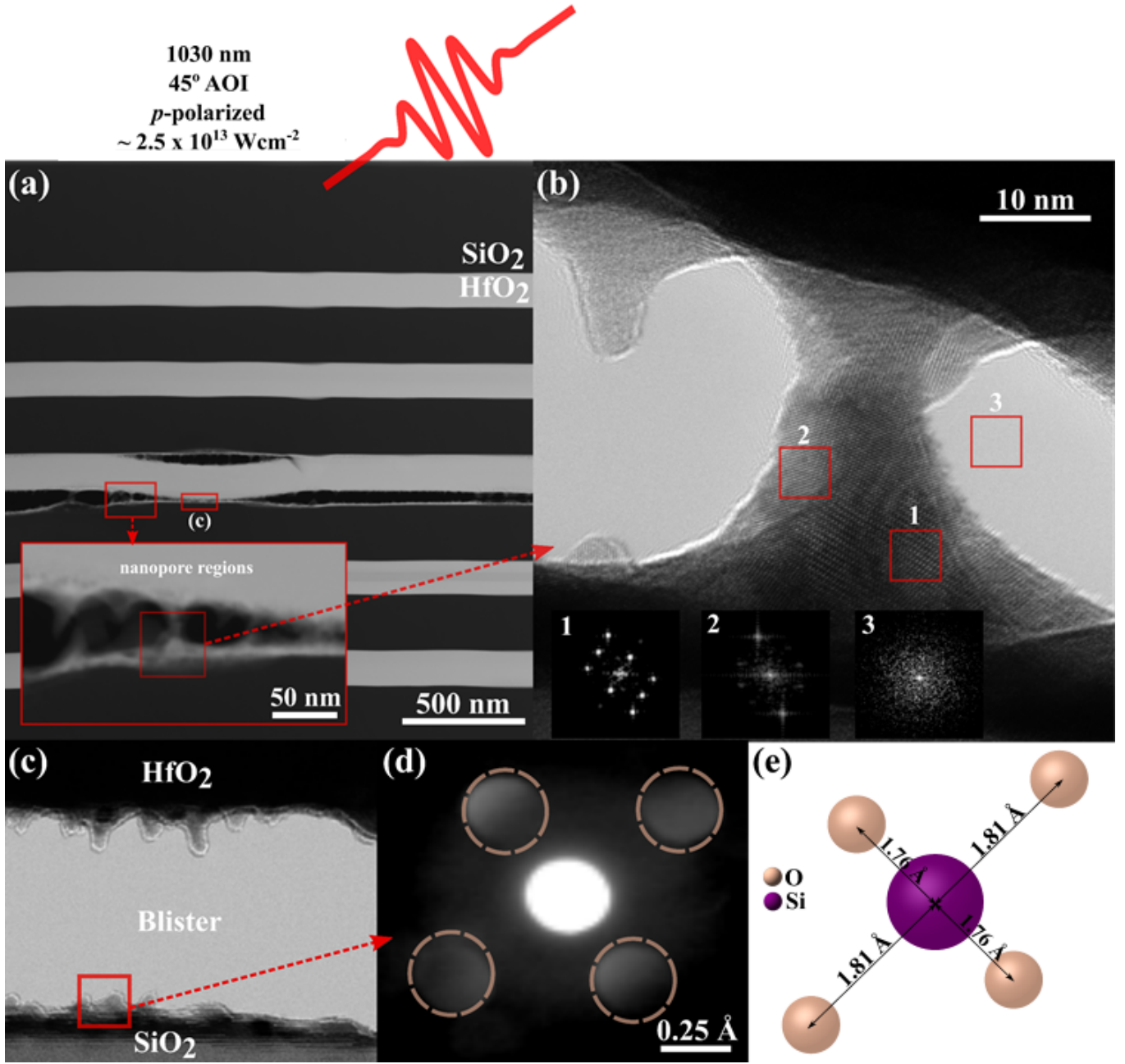


FIG. 7. Laser induced nano structural modification and crystallization at the  $\text{SiO}_2/\text{HfO}_2$  interface. (a) Cross-sectional TEM image of the  $\text{SiO}_2/\text{HfO}_2$  multilayer dielectric mirror after single-shot femtosecond laser irradiation, showing localized interfacial deformation and blister formation. The inset highlights a nanoporous region formed within the  $\text{SiO}_2$  and  $\text{HfO}_2$  layers adjacent to the interface, indicative of rapid volumetric expansion and material rarefaction. (b) High-resolution TEM image of the boxed nanoporous region in (a), revealing nanometer-scale crystalline domains embedded within an amorphous matrix near the  $\text{SiO}_2/\text{HfO}_2$  interface. Fast Fourier transforms (FFTs) from regions 1 and 2 exhibit discrete diffraction spots characteristic of crystalline order, whereas region 3 displays a diffuse amorphous halo. (c) 4D-STEM real-space scan across the modified interface, with the boxed region used for nano diffraction. (d) Nano-diffraction pattern extracted from the laser-modified region using 4D-STEM, showing four well-defined diffraction maxima arranged in a near-square geometry; overlaid guides indicate the measured reciprocal-lattice spacings. (e) Simulated stishovite structure and diffraction viewed along the  $c$ -axis; experimental spacings agree within  $\sim 3\%$ , confirming formation of stishovite at the  $\text{SiO}_2/\text{HfO}_2$  interface.

Such nanoporous features are consistent with strong-field ionization, confined plasma formation, and subsequent pressure-driven relaxation in wide-bandgap oxides. No-

tably, although the electric-field maximum occurs in the first  $\text{HfO}_2$  layer, our strong-field/Keldysh-FDTD simulations show that appreciable free-carrier densities are still

generated within the third  $\text{HfO}_2$  layer, where subsurface plasma confinement and interfacial stress localization favor blister-driven damage initiation beneath the surface [55]. Fig. 7(b) is the high-resolution TEM image of the boxed nanoporous region in (a) which reveals localized nanometer-scale crystalline domains embedded within an otherwise amorphous matrix near the  $\text{SiO}_2/\text{HfO}_2$  interface. Fast Fourier transforms (FFTs) extracted from regions 1 and 2 show discrete diffraction spots characteristic of crystalline order, while region 3 exhibits a diffuse halo typical of amorphous  $\text{SiO}_2$ , confirming the highly localized nature of laser-induced crystallization. To spatially resolve this structural modification with crystallographic sensitivity, a 4D-STEM real-space scan was acquired across the damaged interface, as shown in Fig. 7(c), with the red inset marking the region selected for nano diffraction analysis. The corresponding diffraction pattern extracted from this region, shown in Fig. 7(d), exhibits four pronounced diffraction maxima arranged in a nearly square geometry, signaling the emergence of long-range order within the laser-modified  $\text{SiO}_2$  layer; the overlaid guide highlights the measured reciprocal-lattice spacings. Comparison with simulated diffraction from high-pressure  $\text{SiO}_2$  polymorphs reveals excellent agreement with stishovite viewed along the crystallographic  $c$ -axis, as shown in Fig. 7(e), and Si-O bond lengths (1.76 – 1.81 Å). The experimentally measured diffraction vectors match the simulated stishovite reciprocal spacings within  $\sim 3\%$ , confirming that femtosecond laser excitation locally transforms amorphous  $\text{SiO}_2$  into crystalline stishovite at the  $\text{SiO}_2/\text{HfO}_2$  interface. Together, these observations demonstrate that femtosecond laser excitation induces extreme, highly localized pressure transients at the  $\text{SiO}_2/\text{HfO}_2$  interface, leading to nanoporous void formation, interfacial delamination, and non-equilibrium crystallization of amorphous  $\text{SiO}_2$  into the high-pressure stishovite phase, processes that are inaccessible under equilibrium thermodynamics conditions.

Figure 8 shows a representative SAED pattern acquired from the laser-modified  $\text{SiO}_2$  region at the  $\text{SiO}_2/\text{HfO}_2$  interface. The diffraction pattern consists of multiple discrete spots superimposed on a weak diffuse background, indicating partial crystallization within an amorphous matrix. The dashed concentric rings correspond to calculated reciprocal-lattice spacings of high-pressure  $\text{SiO}_2$  polymorphs, while the indexed reflections (210), (211), (002), (112), and (222) match well with those expected for stishovite. The red-circled diffraction maxima align closely with the simulated ring positions, confirming the presence of nanocrystalline domains with no strong preferred orientation. The measured reciprocal spacings agree with simulated stishovite values within experimental uncertainty of  $\sim 2\%$ , consistent with shock-driven crystallization under ultrafast laser-induced pressure transients.

While the present experimental study isolates single-pulse interactions, we believe that multipulse irradiation is expected to introduce additional and qualitatively dif-

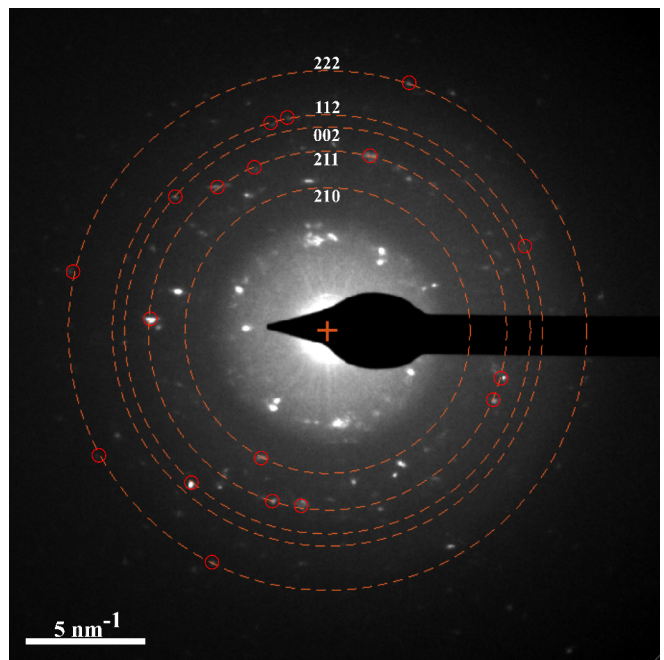


FIG. 8. SAED pattern of laser-induced high-pressure stishovite phases; red circles denote experimental spots, and dashed rings indicate indexed (hkl) planes.

ferent modification pathways. Repeated femtosecond excitation at the same site would initially enhance crystallization by stabilizing laser-induced nuclei and lowering the effective nucleation barrier through defect accumulation, residual densification, and localized field enhancement at pre-existing nanopores and the  $\text{SiO}_2/\text{HfO}_2$  interface. However, with increasing pulse number, cumulative void growth, pressure venting, and thermo-mechanical loading suppress the ultrafast shock confinement required for high-pressure phase formation, driving a transition from localized non-equilibrium crystallization (e.g., stishovite) toward defect-assisted amorphization, interfacial delamination, and eventual catastrophic material removal. A further study with different number of pulses, repetition rate and laser parameters is expected in a future work.

## VI. SUMMARY

We have shown that nanoscale porosity strongly modifies the ultrafast response of silica to femtosecond laser irradiation and can decisively alter its crystallization kinetics. The photoionization rate was computed using the Keldysh formalism with an intensity-dependent bandgap, accounting for the transient narrowing of the  $\text{SiO}_2$  bandgap under strong-field excitation. By combining nonlinear FDTD simulations of energy deposition with atomistic Two-Temperature Molecular Dynamics, we demonstrate that local field enhancement at a nanopore interface concentrates electromagnetic energy

and drives rapid pore collapse. The resulting transient pressure and temperature conditions enable the nucleation and growth of crystalline stishovite on sub-nanosecond timescales, while the final equilibrium temperature in case of twice smaller pore radius and homogeneous systems is well below the one necessary for critical nucleus formation and the systems do not undergo phase transition even after several nanoseconds. The crystallization start was found to be significantly faster in case of porous systems than in homogeneous silica subjected to the same thermal loading.

The simulations reveal that crystallization in porous silica occurs while high pressure is still sustained, allowing the formation of stishovite before pressure relaxation suppresses the transition. In contrast, homogeneous systems exhibit a delayed onset of nucleation, despite reaching comparable average temperature and density. This behavior highlights the critical role of structural inhomogeneities in reducing nucleation barriers and promoting heterogeneous crystallization under strongly nonequilibrium conditions. Within the pore sizes investigated, the acceleration of crystallization is largely insensitive to pore radius, indicating that even nanometer-scale pores are sufficient to trigger this effect.

These results provide a mechanistic explanation for experimental observations of laser-induced crystallization of high-pressure  $\text{SiO}_2$  polymorphs at interfaces and in confined geometries by reproducing the same spatial selectivity and phase outcome. In particular, the formation of stishovite observed experimentally in laser-irradiated silica multilayers and near voided regions is consistent with the pore-mediated energy localization and pressure confinement identified here. More broadly, this work demonstrates that nanoscale porosity can be exploited as an effective control parameter for directing ultrafast solid-state transformations. The framework developed here is directly applicable to other transparent dielectrics and nanoporous materials and provides a predictive basis for engineering laser-driven synthesis of dense and metastable crystalline phases under far-from-equilibrium conditions. Future extensions of this framework could integrate electron dynamics and transient structural disorder to model laser-induced phase transitions in other wide-bandgap systems such as  $\text{Al}_2\text{O}_3$ ,  $\text{TiO}_2$  and  $\text{HfO}_2$ , supporting the predictive design of laser-driven synthesis pathways across diverse dielectric materials.

## ACKNOWLEDGMENTS

This work is part of the FLASH project of PEPR LUMA and was supported by the French National Research Agency, as a part of the France 2030 program, under grant ANR-24-EXLU-0004. It was also funded by a public ANR grant referenced as EUR MANUTECH SLEIGHT-ANR-17-EURE-0026. The numerical calculations were performed using computer resources from GENCI, project gen7041.

## SUPPLEMENTAL MATERIAL

### OVERVIEW

This Supplemental Material provides additional details on the numerical models, simulation parameters, and supporting data referenced in the main text. It includes extended descriptions of the Finite-Difference Time-Domain (FDTD) simulations, and molecular dynamics (MD) setup, together with supplementary figures and more information. All figures are labeled as Fig. S1, S2, etc., and equations as (S1), (S2), etc.

### Appendix A: Introduction

Ultrafast laser irradiation of dielectrics can trigger a broad spectrum of structural responses, from subtle refractive index changes to explosive microstructuring. These responses are conventionally classified into several modification regimes: Type I, corresponding to smooth refractive index changes induced by low-intensity exposure; Type II, characterized by self-organized nanogratings; and Type III, associated with micro-void formation at high fluences. More recently, the introduction of Type X and Type C regimes has expanded this classification to include porous birefringent structures and nonperiodic anisotropic nanocrystals, respectively [9–11]. Each regime depends critically on laser parameters such as fluence, pulse duration, polarization, and repetition rate, revealing different aspects of silica’s nonequilibrium response to ultrafast excitation. In the context of the present work, the Type C and Type X regimes are particularly relevant, as they involve transient formation of nanoporous and nanocrystalline phases, precursors to the ultrafast crystallization processes modeled in this study.

Laser-induced nanoporous structures in silica have emerged as both an intriguing physical phenomenon and a design pathway for photonic materials. Arrays of nanopores aligned perpendicular to the laser polarization create birefringence and enable advanced light-guiding applications [10, 14, 15]. The formation of these nanopores originates from multiphoton ionization, local field enhancement, and plasma-mediated nanocavitation, all of which act synergistically during femtosecond laser exposure [16, 17]. The resulting self-organized structures reflect the interplay between electronic excitation, plasma expansion, and rapid quenching. In porous silica, these processes are further complicated by the material’s spatial heterogeneity, which strongly amplifies local electromagnetic fields near interfaces, making such systems ideal for studying field-driven structural dynamics.

The presence of nanoscale porosity not only enhances local electromagnetic intensity but also reshapes stress and thermal relaxation pathways during ultrafast irradiation. Experiments have shown that voids and nanopores can nucleate under tensile stress conditions where plasma instabilities promote cavitation and mate-

rial separation [18, 19]. These pores often self-organize into nanograting planes with subwavelength periodicity perpendicular to the laser polarization, governed by interference and plasmonic effects [20]. Numerical models coupling Maxwell’s equations with hydrodynamics have reproduced this behavior, predicting bubble formation, pore collapse, and structural decomposition at local temperatures approaching 2000-3000 K [56]. Such coupled optical-mechanical processes provide the physical foundation for the pore collapse and crystallization mechanisms analyzed in the main text, where local field enhancement drives rapid thermomechanical reorganization and phase transition.

MD has become a cornerstone technique for modeling atomic-scale mechanisms in condensed matter systems subjected to nonequilibrium excitation. By numerically integrating Newton’s equations of motion, MD simulations provide direct access to the temporal evolution of atomic configurations under defined thermodynamic and mechanical conditions [21, 25, 57]. Its deterministic formulation and the availability of realistic interatomic potentials make it well suited for investigating phase transitions, defect formation, and structural reorganization. MD has been successfully applied to both crystalline and amorphous oxides, providing insight into atomic rearrangements that remain inaccessible to continuum models or experiments [24, 45]. In the present study, MD complements electromagnetic simulations by capturing the atomistic consequences of localized energy deposition, such as pore collapse, pressure buildup, and the subsequent crystallization dynamics.

The Finite-Difference Time-Domain (FDTD) method, introduced by Yee in 1966 [42], is a widely used numerical approach for solving Maxwell’s equations in both linear and nonlinear optical media. By discretizing space and time on a staggered grid, FDTD can capture the complete temporal and spatial evolution of electromagnetic fields without relying on approximations regarding propagation direction or geometry [28]. Its ability to resolve subwavelength field distributions and incorporate material dispersion makes it particularly effective for studying light confinement and field enhancement near nanoscale features. In this work, the FDTD model computes the nonlinear propagation of femtosecond pulses within nanoporous silica, including intensity-dependent bandgap narrowing and avalanche ionization, to generate a spatially resolved power density map. This distribution serves as the input energy source for subsequent MD simulations, enabling a fully coupled multiscale framework that bridges electromagnetic and atomic dynamics.

The combined use of MD and FDTD enables a self-consistent description of ultrafast energy localization, pore collapse, and crystallization. The FDTD module provides the spatially varying absorbed power density, while the MD module evolves the atomic system under a Two-Temperature Model (TTM) that couples electron and lattice subsystems through electron-phonon interactions. This hybrid approach allows quantitative predic-

tion of temperature rise, pressure buildup, and atomic rearrangement at nanometer and picosecond scales, forming the foundation for the results presented in the main manuscript.

The material presented in this Supplemental Material provides the extended theoretical, computational and experimental background necessary to understand the physical mechanisms discussed in the main article. These sections establish the connection between known ultrafast modification regimes in silica and the newly described pore-assisted crystallization pathway, which is modeled and experimentally validated in the main work.

## Appendix B: Setup

FDTD directly integrates Maxwell’s curl equations in time and space by using the so-called Yee grid, in which the components of the electric and magnetic fields are staggered in both space and time [28, 42]. The electric field is updated at integer multiples of discrete time steps, while the magnetic field is updated at half-integer multiples. These leapfrog updates are applied iteratively at each time step, advancing the fields through time.

The interatomic potential used (modified BKS (Beest-Kramer-Santen) potential [51] (the original BKS [58] with an additional 30-6 Lennard-Jones-type term [59])) consists of a Coulombic term and a Buckingham-type pair potential and was extensively used in dozens of studies to describe both liquid and solid states in silica [60–63]. However, the simulation time with the modified BKS potential does not depend linearly on the number of atoms used in the simulation box, which means that with the increasing number of atoms computational costs get heavier. In this regard, we limit ourselves with a few hundred cubic nanometer volume for the simulation box.

The root mean square deviation (RMSD) between the PRDFs were calculated for all three pairs with the following formula:

$$\text{RMSD} = \sqrt{\frac{1}{M} \sum_{j=1}^M [g_1(r_j) - g_2(r_j)]^2} \quad (\text{S1})$$

where  $M$  is the number of discrete radial grid points, and  $g_1$  and  $g_2$  are the two RDFs being compared.

## Appendix C: Experimental context

Femtosecond laser-induced microexplosions in transparent dielectrics have been shown to generate extreme conditions, pressures up to several TPa and temperatures of thousands of Kelvin, within femtoseconds [64, 65]. When such a pulse is tightly focused into bulk silica glass, the result is a localized plasma, followed by a strong shock wave and rarefaction front. This dynamic compresses the surrounding material into a high-density shell, while

forming a central nanoscale void due to rapid decompression and cavitation.

High-resolution studies using time-resolved microscopy and spectroscopic analysis by Somayaji *et al.* further confirm that nanoscale voids can form in silica even during or after densification [65]. They demonstrated that dense plasma states persist in silica for tens of nanoseconds following ultrafast laser excitation, eventually triggering cavitation and void formation within a compressed matrix.

Rudenko *et al.* also showed through multiphysics simulations that laser-induced voids are a product of cavitation in regions with subcritical but high electron densities, where surrounding regions undergo thermomechanical compaction [56].

The phenomenon of coexisting densified regions and nanopores has been modeled and observed experimentally across multiple studies. In compressed glass systems, nanopores formed due to laser-induced pressure accumulation have been found to reside inside or adjacent to regions that experience significant compaction, even at the nanometric scale [66].

Additionally, FDTD simulations by Naseri *et al.* support the existence of densified shells surrounding voids, emphasizing that void arrays can be consistently formed via linear optical mechanisms that naturally result in high-density peripheries [67].

Thermodynamically, the formation of voids in a supercompressed matrix is permissible due to local instabilities. The highly non-equilibrium state induced by ultrafast energy deposition exceeds the glass transformation temperature and bypasses conventional crystallization pathways, enabling phase coexistence. While the average density is slightly reduced by the presence of voids, the surrounding matrix can locally reach or exceed the density of high-pressure polymorphs.

Grujicic *et al.* conducted molecular-level simulations supported by DFT calculations. They showed that ballistic impact on silica can induce localized densification and crystallization [46]. They also demonstrated that under pressures around 50 GPa and in the presence of shear, stishovite becomes the most stable form of  $\text{SiO}_2$  and the energy barrier associated to the transition from silica glass to stishovite is the smallest.

In our recent study femtosecond laser pulses were used to irradiate multilayer dielectric stacks of silica and hafnium oxide. Post-irradiation analyses revealed the formation of a blister in the central region of the top silica layer, while the boundaries of this blister remained adhered to the underlying  $\text{HfO}_2$  interface [45]. Intriguingly, these blistered structure showed clear signatures of several crystalline silica polymorphs, including not only stishovite but also higher-pressure phases such as seifertite and pyrite-type  $\text{SiO}_2$ , in both the compressed edges and across the modified silica layer. This supports the notion that highly densified regions of silica, with densities approaching or exceeding that of stishovite, can indeed be formed under ultrafast laser conditions. Such

a blister may also be the macroscopic analog of a pore. A large void within silica, under the influence of a spatially Gaussian laser pulse, can act as a low-density inclusion around which energy absorption and mechanical compression are strongly enhanced. FDTD simulations corroborate this, showing enhanced field localization at dielectric interfaces, especially near concave boundaries such as pore edges.

The metastable existence of such high-density phases under ambient recovery has been demonstrated experimentally. Alam *et al.* showed that exposing micron-sized  $\text{SiO}_2$  particles to laser heating in air produces not just stishovite, but even higher-pressure polymorphs such as the  $\text{CaCl}_2$ -type and  $\alpha$ - $\text{PbO}_2$ -type structures [68]. This highlights the broader relevance of laser-driven densification in silica and supports the assumption underlying our model under similar conditions.

Taken together, these findings provide strong physical and experimental justification for the initial conditions used in our simulations. They suggest that localized, high-density silica domains containing transient nanopores can indeed emerge under realistic ultrafast laser excitation scenarios. Such configurations can be experimentally created by single or multipulse femtosecond laser irradiation at intensities exceeding  $10^{13} \text{ W/cm}^2$ , or through adapted pressure-quenching protocols. Therefore, this model captures essential features of real-world laser-matter interactions and provides a framework for simulating pore collapse and energy diffusion phenomena.

#### Appendix D: Results

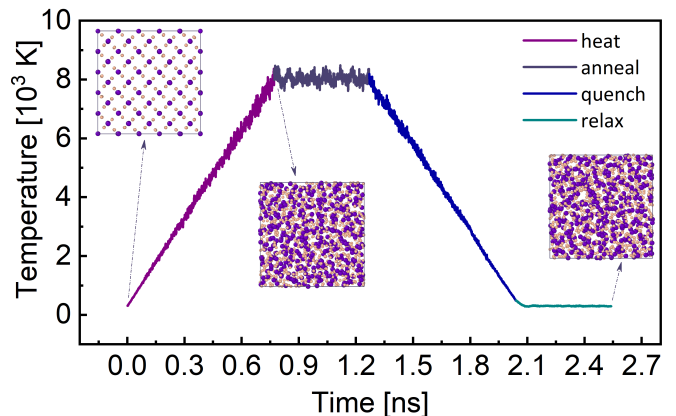


FIG. S1. Temperature evolution in time during the amorphization of stishovite. A standard heat-quench method was used with canonical ensemble. The annealing stage is applied after heating to ensure a total removal of crystalline memory from the already amorphized system. A relaxation stage is applied to remove any residual stress after the quench. The snapshots show the initial ordered (*c*-axis) and the disordered configurations during the amorphization process.

Figure S1 shows the temporal evolution of temperature during the amorphization by a heat-anneal-quench-relax protocol. The snapshots depicted in the figure show the initial crystalline and disordered atomic configurations after heating and after equilibration.

Figure 2 presents the distribution of free electron density in both 2-nm-radius and 1-nm-radius structures for the central slices. The free electron density is strongly modulated by the presence of the pore for both pore sizes, reaching to a maximum value right at the pore surface boundary of approximately  $4 \times 10^{22} \text{ cm}^{-3}$ . The highest electron densities are localized at the pore surface regions aligned with the laser polarization direction. The discontinuity in permittivity at the dielectric-pore interface leads to local electric field amplification, which enhances nonlinear ionization processes and results in higher electron densities near the pore boundary.

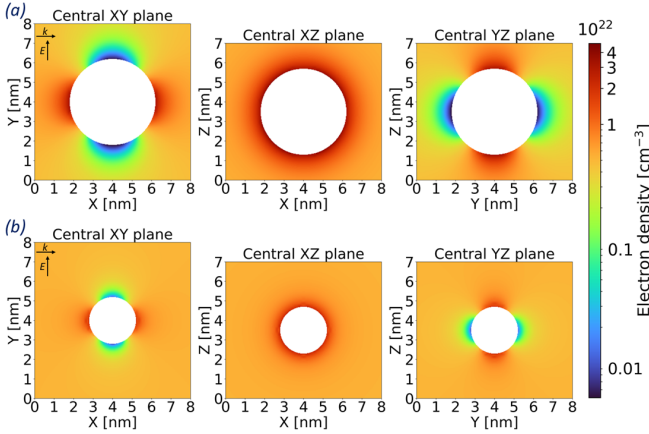


FIG. S2. Central slices of free electron density distribution after laser irradiation, smoothed for better visualization, for the structure with a (a) 2-nm-radius pore and (b) 1-nm-radius pore.

The overall patterns of free electron density distributions are clearly similar to the ones of the absorbed energy density. For the 2-nm-radius pore, the spatial extension of the high-density electron region around the pore shell is broader and the maximum values of density are distributed over a larger surface area. In contrast, the 1-nm-radius pore shows a narrower enhanced shell around the pore. The higher curvature for 1-nm pore leads to more localized field concentration leading to a sharper and more confined plasma region around the pore interface.

Figure S3 presents the spatial distribution of intensity in the 2-nm pore structure (a), together with the corresponding bandgap distribution (b), obtained by mapping the local intensity to the intensity-dependent bandgap (top panel in Fig. 2). The snapshots correspond to the instant time at which the incident laser pulse reaches its peak intensity in the FDTD simulation.

The intensity map reveals pronounced field enhancement localized at the pore boundary. The enhancement is

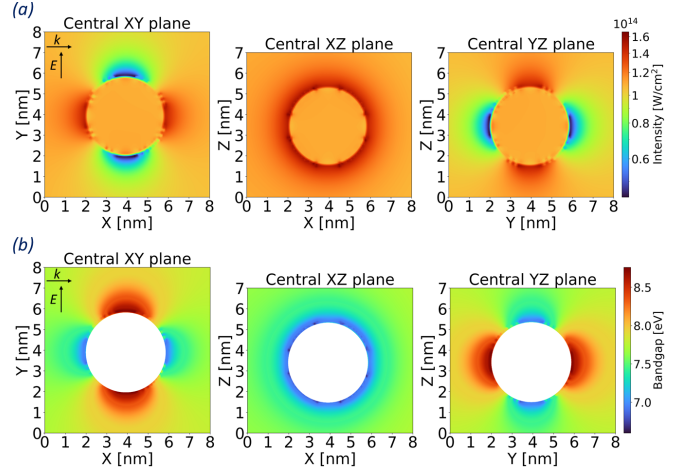


FIG. S3. (a) Smoothed intensity distribution of 2-nm structure taken from FDTD data when the laser pulse intensity was at its peak. (b) The corresponding bandgap distribution obtained from the data of intensity versus bandgap.

strongly polarization-dependent and follows the expected pattern for a subwavelength cavity, with hot spots forming along the direction of the electric field, similar to absorbed energy and free electron density maps. The maximum local intensity exceeds the incident peak value by a factor of around 1.6 in the hottest spots of the pore boundaries, indicating significant near-field enhancement at silica interface.

The corresponding bandgap distribution demonstrates a clear spatial correlation between field enhancement and bandgap renormalization. Regions of maximum intensity coincide with the strongest bandgap shrinkage, showing the highly nonlinear response of the material. At the hottest spots along the pore boundary, the bandgap decreases from its initial value of 8.9 eV to approximately 6.6 eV. This localized bandgap shrinkage is confined to a narrow region around the interface, corresponding to the steep spatial gradients of the electromagnetic field. Away from the pore boundary, where the intensity relaxes toward the background level, the bandgap correspondingly recovers toward its higher value.

Even at intensities close to approximately  $4.5 \times 10^{13} \text{ W/cm}^2 - 1.65 \times 10^{14} \text{ W/cm}^2$  range, relevant to our simulations, the dynamic bandgap increases the calculated rate at the hottest spots of the pore boundaries by a factor of up to about 5 compared to the static-bandgap case, indicating that field-driven gap renormalization significantly amplifies free-carrier generation. One should also note that while the ratio of ionization rate between the pore boundary and background homogeneous region was approximately 4 in case of static bandgap, the same ratio reached to approximately 10 in case of dynamic bandgap. This enhancement directly affects the spatial distribution of absorbed energy obtained from FDTD simulations, strengthening local electromagnetic confinement at pore interfaces and ultimately accelerating the

thermomechanical collapse of the surrounding silica network.

This spatially inhomogeneous bandgap modulation implies that ionization and carrier generation will preferentially initiate at the pore boundary, particularly along the polarization axis. The strong localization suggests that even moderate incident intensities can trigger substantial electronic modification in nanoscale regions due to near-field enhancement. Such localized bandgap reduction may further increase absorption, potentially leading to positive feedback in carrier generation and energy deposition.

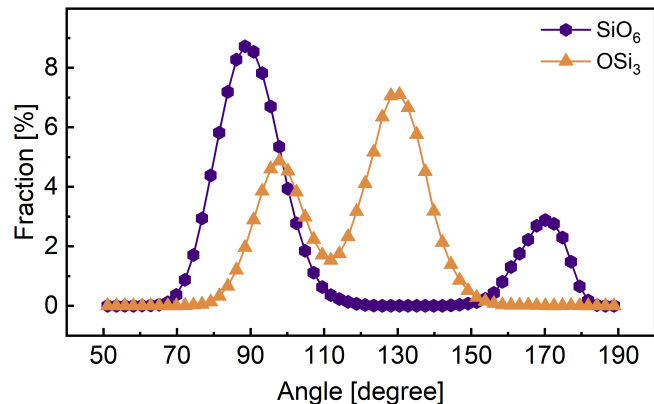


FIG. S4. Bond-angle distribution in  $\text{SiO}_6$  and  $\text{OSi}_3$  coordination units of the crystallized system 2 ns after the irradiation. The peaks at  $90^\circ$  and  $170^\circ$  for  $\text{SiO}_6$  correspond to adjacent and trans ligands, respectively. The same way the peaks at  $97^\circ$  and  $130^\circ$  show the edge sharing and corner-sharing connections.

Figure S4 presents the bond-angle distribution in the crystallized system for O-Si-O and Si-O-Si angles within  $\text{SiO}_6$  and  $\text{OSi}_3$  coordination units, respectively. These distributions offer insights into both the local geometry of the structural units and the connectivity of the resulting silicate network after crystallization into stishovite. The O-Si-O angle distribution for  $\text{SiO}_6$  units shows a prominent peak centered around  $90^\circ$ , with a secondary, broader feature near  $170^\circ$ , in strong agreement with other

studies [69, 70]. These features are characteristic of octahedral coordination in stishovite where the first peak corresponds to O-Si-O angle between adjacent ligands, while the second, lower peak corresponds to angles between trans ligands.

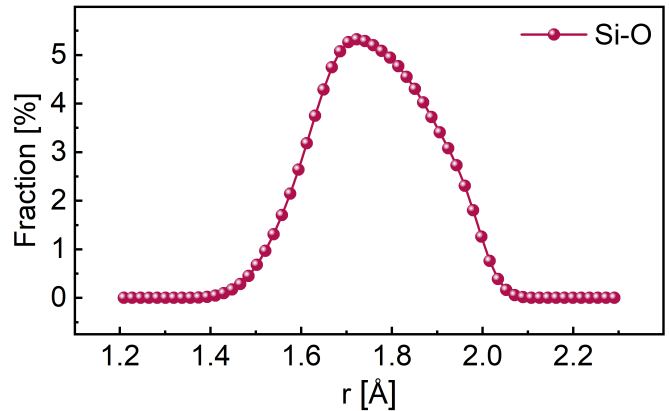


FIG. S5. Si-O bond length distribution, peaked around  $1.73 \text{ \AA}$ , within  $\text{SiO}_6$  coordination units in the crystallized system at a final pressure of 27 GPa.

On the other hand, the Si-O-Si angle distribution for  $\text{OSi}_3$  units displays a bimodal structure, with distinct peaks around  $97^\circ$  and  $130^\circ$ . These angles reflect the ways in which oxygen atoms bridge between neighboring Si atoms. The peak at  $97^\circ$  is typical of edge-sharing octahedra in stishovite, whereas the broader peak at  $130^\circ$  arises from corner-sharing connections [69, 70]. The presence of these two peaks shows the dual nature of the connectivity in stishovite crystal.

Figure S5 presents the distribution of Si-O bond lengths within  $\text{SiO}_6$  coordination units in the crystallized system at a final pressure of 27 GPa. The distribution exhibits a single, well-defined peak centered at  $1.73 \text{ \AA}$ , indicating a narrow spread of bond lengths consistent with the formation of a structurally ordered phase. The observed bond length is in close agreement with experimental measurements of stishovite under high-pressure conditions [71].

- 
- [1] W. Pabst and E. Gregorová, Elastic properties of silica polymorphs - a review, *Silikaty* **57**, 167 (2013).
  - [2] S. Stishov and S. Popova, A new modification of silica, *Geokhimiya* **10**, 873 (1961).
  - [3] M. Miyahara, E. Ohtani, A. Yamaguchi, S. Ozawa, T. Sakai, and N. Hirao, Discovery of coesite and stishovite in eucrite, *Proc. Natl. Acad. Sci. U.S.A.* **111** (2014).
  - [4] Z. Rehman, S. Ullah, H. Qayyum, M. Irfan, K. A. Tran, H. Suk, A. Qayyum, and K. A. Janulewicz, Phase transformations initiated by optical breakdown in bulk of fused silica, *Opt. Laser Technol.* **134**, 106630 (2021).
  - [5] L. Zheng, Q. An, R. Fu, S. Ni, and S. Luo, Densification of silica glass at ambient pressure, *J. Chem. Phys.* **125**, 154511 (2006).
  - [6] K. Mishchik, *Ultrafast laser-induced modification of optical glasses: a spectroscopy insight into the microscopic mechanisms*, Ph.D. thesis (2012).
  - [7] R. M. Vignes, T. F. Soules, J. S. Stolken, R. R. Settgast, S. Elhadj, and M. J. Matthews, Thermomechanical modeling of laser-induced structural relaxation and deformation of glass: Volume changes in fused silica at high temperatures, *J. Am. Ceram. Soc.* **96**, 137 (2013).
  - [8] R. Stoian and J.-P. Colombier, Advances in ultrafast laser structuring of materials at the nanoscale, *Nanophotonics* **9**, 4665 (2020).
  - [9] N. Shchedrina, M. Sosa, M. Cavillon, and M. Lancry,

- Properties, mechanisms, and perspectives of ultrafast laser modifications in silicate glass volume, *J. Appl. Glass Sci.* (2025).
- [10] M. Sakakura, Y. Lei, L. Wang, Y.-H. Yu, and P. G. Kazansky, Ultralow-loss geometric phase and polarization shaping by ultrafast laser writing in silica glass, *Light Sci. Appl.* **9** (2020).
- [11] K. Miura, J. Qiu, T. Mitsuyu, and K. Hirao, Space-selective growth of frequency-conversion crystals in glasses with ultrashort infrared laser pulses, *Opt. Lett.* **25**, 408 (2000).
- [12] A. Gleason, C. Bolme, H. Lee, B. Nagler, E. Galtier, D. Milathianaki, R. Kraus, J. Eggert, D. Fratanduono, G. Collins, R. Sandberg, W. Yang, and W. Mao, Ultrafast visualization of crystallization and grain growth in shock-compressed SiO<sub>2</sub>, *Nat. Commun.* **6**, 8191 (2015).
- [13] G. T. T. Trang and P. H. Kien, Study of structure transition and crystallization of amorphous silica under compression, *VNU J. Sci. Math. Phys.* **36** (2020).
- [14] M. Lancry, B. Poumellec, J. Canning, K. Cook, J. Poulin, and F. Brisset, Ultrafast nanoporous silica formation driven by femtosecond laser irradiation, *Laser Photonics Rev.* **7**, 953 (2013).
- [15] G. Shayeganrad, X. Chang, H. Wang, C. Deng, Y. Lei, and P. Kazansky, High damage threshold birefringent elements produced by ultrafast laser nanostructuring in silica glass, *Opt. Express* **30**, 41002 (2022).
- [16] A. Rudenko, H. Ma, V. Veiko, J.-P. Colombier, and T. Itina, On the role of nanopore formation and evolution in multi-pulse laser nanostructuring of glasses, *Appl. Phys. A* **124**, 1 (2017).
- [17] M. Lancry, B. Poumellec, K. Cook, and J. Canning, Nanogratings and molecular oxygen formation during femtosecond laser irradiation in silica (2011) p. C229.
- [18] M. Lancry, J. Canning, K. Cook, M. Heili, D. Neuville, and B. Poumellec, Nanoscale femtosecond laser milling and control of nanoporosity in the normal and anomalous regimes of GeO<sub>2</sub>-SiO<sub>2</sub> glasses, *Opt. Mater. Express* **6**, 321 (2016).
- [19] A. Champion, M. Beresna, P. Kazansky, and Y. Belouard, Stress distribution around femtosecond laser affected zones: effect of nanogratings orientation, *Opt. Express* **21**, 24942 (2013).
- [20] Y. Shimotsuma, P. G. Kazansky, J. Qiu, and K. Hirao, Self-organized nanogratings in glass irradiated by ultrashort light pulses, *Phys. Rev. Lett.* **91**, 247405 (2003).
- [21] D. Iabbaden, J. Amodeo, C. Fusco, F. Garrelie, and J.-P. Colombier, Molecular dynamics simulation of structural evolution in crystalline and amorphous CuZr alloys upon ultrafast laser irradiation, *Phys. Rev. Mater.* **6**, 126001 (2022).
- [22] D. Iabbaden, J. Amodeo, C. Fusco, F. Garrelie, and J.-P. Colombier, Dynamics of Cu-Zr metallic glass devitrification under ultrafast laser excitation revealed by atomistic modeling, *Acta Mater.* **263**, 119487 (2023).
- [23] D. Iabbaden, A. Tsaturyan, J.-M. Raulot, and J.-P. Colombier, Nonequilibrium electronic properties and stability consequences in metallic crystalline binary alloys under ultrafast laser excitation, *J. Alloys Compd.* **1010**, 177175 (2025).
- [24] H. Nguyen, A. Tsaturyan, S. Sao Joao, R. Dwivedi, A. Yedigaryan, C. d'Amico, E. Kachan, J.-P. Colombier, G. Kermouche, and R. Stoian, Quantitative mapping of transient thermodynamic states in ultrafast laser nanostructuring of quartz, *Ultrafast Sci.* **4** (2024).
- [25] A. Yedigaryan, E. Kachan, and J.-P. Colombier, Thermodynamic pathways of silica glass densification by molecular dynamics simulations, *Appl. Phys. A* **131**, 1 (2025).
- [26] P. Dominic, D. Iabbaden, F. Bourquard, S. Reynaud, A. Weck, J.-P. Colombier, and F. Garrelie, Ultrafast laser-induced sub-100 nm structures on tungsten surfaces: stretched liquid dynamics insights, *Phys. Status Solidi A* **221**, 2300703 (2024).
- [27] M. Prudent, D. Iabbaden, F. Bourquard, S. Reynaud, Y. Lefkir, A. Borroto, J.-F. Pierson, F. Garrelie, and J.-P. Colombier, High-density nanowells formation in ultrafast laser-irradiated thin film metallic glass, *Nano-Micro Lett.* **14**, 1 (2022).
- [28] A. Taflove and S. C. Hagness, *Computational Electrodynamics: The Finite-Difference Time-Domain Method*, 3rd ed. (Artech House, 2005).
- [29] A. F. Oskooi, D. Roundy, M. Ibanescu, P. Bermel, J. D. Joannopoulos, and S. G. Johnson, Meep: A flexible free-software package for electromagnetic simulations by the fdtd method, *Comput. Phys. Commun.* **181**, 687 (2010).
- [30] A. Rudenko, J.-P. Colombier, S. Höhm, A. Rosenfeld, J. Krüger, J. Bonse, and T. Itina, Spontaneous periodic ordering on the surface and in the bulk of dielectrics irradiated by ultrafast laser: A shared electromagnetic origin, *Sci. Rep.* **7** (2017).
- [31] L. V. Keldysh, Ionization in the field of a strong electromagnetic wave, *Sov. Phys. JETP* **20**, 1307 (1965).
- [32] S. I. Anisimov, B. L. Kapeliovich, and T. L. Perel'Man, Electron emission from metal surfaces exposed to ultrashort laser pulses, *Sov. J. Exp. Theor. Phys.* **39**, 375 (1974).
- [33] M. W. Finnis, P. Agnew, and A. J. E. Foreman, Thermal excitation of electrons in energetic displacement cascades, *Phys. Rev. B* **44**, 567 (1991).
- [34] H. Hakkinen and U. Landman, Superheating, melting, and annealing of copper surfaces, *Phys. Rev. Lett.* **71**, 1023 (1993).
- [35] C. Schaefer, H. M. Urbassek, and L. V. Zhigilei, Metal ablation by picosecond laser pulses: A hybrid simulation, *Phys. Rev. B* **66**, 115404 (2002).
- [36] D. S. Ivanov and L. V. Zhigilei, Combined atomistic-continuum modeling of short-pulse laser melting and disintegration of metal films, *Phys. Rev. B* **68**, 064114 (2003).
- [37] W. Yuan and T. Sizyuk, Ablation study in gold irradiated by single femtosecond laser pulse with electron temperature dependent interatomic potential and electron-phonon coupling factor, *Laser Phys.* **31**, 036002 (2021).
- [38] [https://docs.lammps.org/fix\\_ttm.html](https://docs.lammps.org/fix_ttm.html).
- [39] S. Plimpton, Fast parallel algorithms for short-range molecular dynamics, *J. Comput. Phys.* **117**, 1 (1995).
- [40] D. Duffy and A. Rutherford, Including the effects of electronic stopping and electron-ion interactions in radiation damage simulations, *J. Phys.: Condens. Matter* **19**, 016207 (2006).
- [41] A. M. Rutherford and D. M. Duffy, The effect of electron-ion interactions on radiation damage simulations, *J. Phys.: Condens. Matter* **19**, 496201 (2007).
- [42] K. S. Yee, Numerical solution of initial boundary value problems involving Maxwell's equations in isotropic media, *IEEE Trans. Antennas. Propag.* **14**, 302 (1966).
- [43] V. Fedorov and J.-P. Colombier, Light-matter interaction at rough surfaces: A morphological perspective on laser-

- induced periodic surface structures, *Phys. Rev. B* **110** (2024).
- [44] A. Tsaturyan, E. Kachan, R. Stoian, and J.-P. Colombier, Unraveling the electronic properties in  $\text{SiO}_2$  under ultrafast laser irradiation, *npj Comput. Mater.* **10** (2024).
- [45] M. Y. Noor, A. Yedigaryan, G. Calderon, A. Tsaturyan, E. Kachan, J. Hwang, C. S. Menoni, J.-P. Colombier, and E. Chowdhury, Mimicking the earth core conditions with ultrafast laser materials interaction, arXiv:2602.22460 (2026).
- [46] M. Grujicic, J. Snipes, S. Ramaswami, R. Yavari, and B. Cheeseman, Densification and devitrification of fused silica induced by ballistic impact: A computational investigation, *J. Nanomater.* **2015**, 1 (2015).
- [47] L. Sudrie, A. Couairon, M. Franco, B. Lamouroux, B. Prade, S. Tzortzakis, and A. Mysyrowicz, Femtosecond laser-induced damage and filamentary propagation in fused silica, *Phys. Rev. Lett.* **89**, 186601 (2002).
- [48] A. Couairon, L. Sudrie, M. Franco, B. Prade, and A. Mysyrowicz, Filamentation and damage in fused silica induced by tightly focused femtosecond laser pulses, *Phys. Rev. B* **71**, 125435 (2005).
- [49] R. W. Boyd, *Nonlinear Optics*, 3rd ed. (Academic Press, 2008).
- [50] I. Burakov, N. Bulgakova, R. Stoian, A. Rosenfeld, and I. Hertel, Theoretical investigations of material modification using temporally shaped femtosecond laser pulses, *Appl. Phys. A* **81**, 1639 (2005).
- [51] I. Saika-Voivod, F. Sciortino, and P. H. Poole, Computer simulations of liquid silica: Equation of state and liquid-liquid phase transition, *Phys. Rev. E* **63**, 011202 (2000).
- [52] A. Stukowski, Visualization and analysis of atomistic simulation data with OVITO – the Open Visualization Tool, *Model. Simul. Mater. Sci. Eng.* **18**, 015012 (2010).
- [53] R. Becker and W. Döring, Kinetische behandlung der keimbildung in übersättigten dämpfen, *Ann. Phys.* **24**, 719 (1935).
- [54] B. Pommellec, M. Cavillon, and M. Lancry, Electrostatic interpretation of phase separation induced by femtosecond laser light in glass, *Crystals* **13** (2023).
- [55] M. Y. Noor, E. Deangelis, S. Zhang, C. Kuz, J. Twardowski, A. Davenport, C. S. Menoni, and E. Chowdhury, Pulse duration dependent effects of ultrafast laser induced damage on a 1030 nm multi-layer dielectric mirror for high repetition rate, high average power laser systems, *Opt. Mater. Express* **15**, 212 (2025).
- [56] A. Rudenko, J.-P. Colombier, and T. E. Itina, Nanopore-mediated ultrashort laser-induced formation and erasure of volume nanogratings in glass, *Phys. Chem. Chem. Phys.* **20**, 5887 (2018).
- [57] I. S. Omeje, D. Iabbaden, P. Ganster, and T. E. Itina, Reactive atomistic insights into oxidation dynamics and wettability of ultrafast laser-treated titanium surfaces, *Surf. Interfaces* **68**, 106537 (2025).
- [58] B. W. H. van Beest, G. J. Kramer, and R. A. van Santen, Force fields for silicas and aluminophosphates based on ab initio calculations, *Phys. Rev. Lett.* **64**, 1955 (1990).
- [59] G. Mie, Zur kinetischen theorie der einatomigen körper, *Ann. Phys.* **316**, 657 (1903).
- [60] B. Karki, D. Bhattarai, and L. Stixrude, First-principles simulations of liquid silica: Structural and dynamical behavior at high pressure, *Phys. Rev. B* **76** (2007).
- [61] B. Karki, D. Bhattarai, M. Mookherjee, and L. Stixrude, Visualization-based analysis of structural and dynamical properties of simulated hydrous silicate melt, *Phys. Chem. Miner.* **37**, 103 (2009).
- [62] A. Saksengwijit and A. Heuer, Finite-size effects in silica: a landscape perspective, *J. Phys.: Condens. Matter* **19** (2007).
- [63] P. K. Hung, N. V. Hong, and L. T. Vinh, Diffusion and structure in silica liquid: a molecular dynamics simulation, *J. Phys.: Condens. Matter* **19** (2007).
- [64] E. G. Gamaly, L. Rapp, V. Roppo, S. Juodkakis, and A. V. Rode, Generation of high energy density by fs-laser-induced confined microexplosion, *New J. Phys.* **15**, 025018 (2013).
- [65] M. Somayaji, M. Bhuyan, F. Bourquard, P. Velpula, C. d'Amico, J.-P. Colombier, and R. Stoian, Multiscale electronic and thermomechanical dynamics in ultrafast nanoscale laser structuring of bulk fused silica, *Sci. Rep.* **10** (2020).
- [66] P. Velpula, M. Bhuyan, F. Courvoisier, H. Zhang, J.-P. Colombier, and R. Stoian, Spatio-temporal dynamics in nondiffractive bessel ultrafast laser nanoscale volume structuring, *Laser Photonics Rev.* **10**, 230 (2016).
- [67] N. Naseri, M. Crenshaw, A. Samarbakhsh, and L. Ramunno, A novel approach to study laser induced void array formation in fused silica, arxiv:2401.14407 (2023).
- [68] M. Alam, T. DebRoy, R. Roy, and E. Brevail, High-pressure phases of  $\text{SiO}_2$  made in air by Femtosecond-Derjaguin laser process, *Appl. Phys. Lett.* **53**, 1687 (1988).
- [69] N. T. Nhan, G. T. T. Trang, T. Itaka, and N. V. Hong, Crystallization of amorphous silica under compression, *Can. J. Phys.* **97**, 1133 (2019).
- [70] M. Misawa, E. Ryuo, K. Yoshida, R. K. Kalia, A. Nakano, N. Nishiyama, F. Shimojo, P. Vashishta, and F. Wakai, Picosecond amorphization of  $\text{SiO}_2$  stishovite under tension, *Sci. Adv.* **3**, e1602339 (2017).
- [71] T. Sato and N. Funamori, High-pressure structural transformation of  $\text{SiO}_2$  glass up to 100 GPa, *Phys. Rev. B* **82**, 184102 (2010).